

Chapter 13

Modeling Mid-Infrared Fiber Laser Systems

Robert I. Woodward and Martin Gorjan

ABSTRACT

Mid-IR fibre lasers are complex nonlinear dynamical systems, involving interplay between many physical phenomena and offering vast design freedom. The development of numerical models to simulate laser behaviour is therefore an invaluable tool, both to optimize output performance and to advance understanding of novel laser transitions. Such insight would be significantly slower and more costly to obtain (or indeed, impossible) through laboratory experimentation alone. In this Chapter, we offer a general introduction to various topics in mid-IR fibre laser modelling, with a particular emphasis on rate equation simulations. Complete formalisms are developed from first principles, notably using a matrix approach which is well suited for complex mid-IR transitions, and we discuss practical solution strategies. Case studies are presented for CW, Q-switched and gain-switched lasers, considering both the dysprosium and erbium ion. The second part of the Chapter then considers thermal modelling to identify cooling strategies for high-power systems and ultrashort pulse simulations for modelling mode-locked lasers.

KEYWORDS

Modelling, Simulations, Spectroscopy, Rate equations, Heat equation, Non-linear Schrödinger equation

13.1 INTRODUCTION

The aim of theoretical laser modelling in scope of the present chapter is to predict the behaviour of a fibre laser from the properties of its constituent parts and other design parameters, in order to achieve faster and/or deeper insight than is generally possible by experimentation alone. As such it is not a substitute but a valuable supplement to experimental procedures. The relation goes both ways: knowledge of many spectroscopic parameters is required as an input to the model and must be obtained beforehand. The output of the model can, on the other hand, be used to study the individual or combined effects of any of those parameters, in order to provide further validation for the parameters' values, as well as offering invaluable guidance in laser system design and optimization. The output of such model would typically include fairly common laser operation parameters such as the laser output power and efficiency, threshold power of the

laser oscillator, signal gain of the laser amplifier, as well as amplified spontaneous emission (ASE) as the source or background to the main signal. However, many more output parameters can be accessed as part of the solution.

Laser rate equation models are commonly applied to simulate the evolution of the power and energy dynamics of fibre (and other types of) laser systems. Typically, mid-IR laser transitions in rare-earth-doped media are more spectroscopically complicated than in the near-IR, due to the need to consider many energy levels. Numerous transitions can be relevant between these levels, including cross-relaxation and energy transfer processes between multiple ions (e.g. due to heavy doping or co-doping designs). For this reason, defining the rate equation model in terms of a scalable matrix formulation is particularly well suited for simulating mid-IR systems. The construction of such a model, along with discussion on how to prepare the input data and the methods to find its solutions in steady-state and transient (i.e. time-dependent) regimes, constitute the central part of the present Chapter.

These models have already proven useful in a number of mid-IR fibre laser systems. For example, in heavily-doped Er:ZBLAN, numerical modelling enabled recalibration of the interionic parameters that seem to appear significantly weaker than previously measured in the bulk material [1, 2]. Such procedures also permitted the estimation of cross section values for previously unmeasured excited state absorption (ESA) transitions in Er:ZBLAN [3]. In situations where spectroscopic parameters were already well-known, simulations have been shown to be a powerful tool for optimising laser cavity designs for record tunability and output power [4], in addition to exploring pulsed operating regimes by considering dynamical solutions [5, 6]. After introducing the rate equation method in Section 13.2, we provide case studies in both steady-state and dynamical regimes by applying the model to both a multi-level Er system and a much simpler two-level Dy transition, which is presented first as a more accessible introduction to practical simulations.

While rate equation modelling is perhaps the most important technique for simulating fibre lasers, there are a number of other theoretical tools which can be used to gain further insight into laser operation. For example, thermomechanical failure of ZBLAN fibres at high power is a current limitation to power scaling of mid-IR lasers. Therefore, calculation of heat flow in fibres through thermal modelling can enable improved designs and cooling strategies, as discussed in Section 13.3. Additionally, the scope of applications for mid-IR lasers is further broadened by mode-locking them to produce ultrashort pulses of light. In this case, it becomes important to consider the phase, in addition to the amplitude of light, in order to simulate mode-locked systems, which is the topic of Section 13.4. Finally, the Chapter is concluded in Section 13.5 with an outlook of the opportunities that lie ahead.

13.2 RATE EQUATION MODELLING

The laser rate equations are differential equations that describe the evolution of power / energy in laser modes and atomic (ionic, molecular etc.) systems in both time and space, i.e. along the fibre length. A more thorough treatment of the subject in general can be found in the literature, e.g. Ref. [7], and it is noted that numerous works have already considered detailed rate equation modelling of near-IR transitions, e.g. Refs [8, 9, 10]. In this section, the basic concepts will be gradually introduced on two mid-IR systems: first, a simple 2-level Dy system and then a more complex multi-level Er system.

It is worth mentioning here that in the rate equation model, only optical power (density) is taken into account, via essentially counting the number of photons of certain energy, i.e. wavelength, in the fibre core / modes (volume). Therefore, optical properties stemming from the wave nature of light, including phase, are not included. Fibre guided modes must be calculated separately and are then accounted for with a mode *overlap factor*, as explained in the later sections. Additionally, it should be noted that rate equations technically describe a statistical evolution averaged over many ions within the doped fibre: this assumes all ions behave identically and thus neglects local variations in the fibre and ionic clustering effects. Extended models have been proposed to relax some of these assumptions [11], but have yet to be applied for mid-IR fibre systems and are beyond the scope of this chapter.

13.2.1 Definition of Optical Channels

Before formulating a system of rate equations, the concept of *optical channels* is introduced, which defines how light at different wavelengths is handled. As with any numerical model, continuous quantities such as wavelength must be discretised, i.e. sampled. For example, one could define a numerical grid of many equally spaced wavelength values that cover the spectral region of interest. The simulation would then proceed by solving the rate equations simultaneously for all these different wavelengths, since they are coupled by the broad absorption/emission cross sections for transitions between levels. However, this approach quickly becomes computationally expensive when dealing with hundreds of simultaneous equations and many possible interactions.

A more practical solution, therefore, is to carefully choose a small number of optical channels—i.e. narrow wavelength regions at various salient wavelengths. At the simplest level, this could be a monochromatic pump channel at the pump wavelength and a monochromatic signal channel at the wavelength where the laser is expected to lase. Fig. 13.1 illustrates this concept with the simple example of the in-band-pumped Dy laser (${}^6H_{13/2} \rightarrow {}^6H_{15/2}$ transition): we consider the case for pumping with a 2.83 μm laser and assume 3.15 μm narrowband cavity mirrors (e.g. FBGs) that define the signal wavelength. If a laser with broadband mirrors is being simulated, where the lasing wavelength is

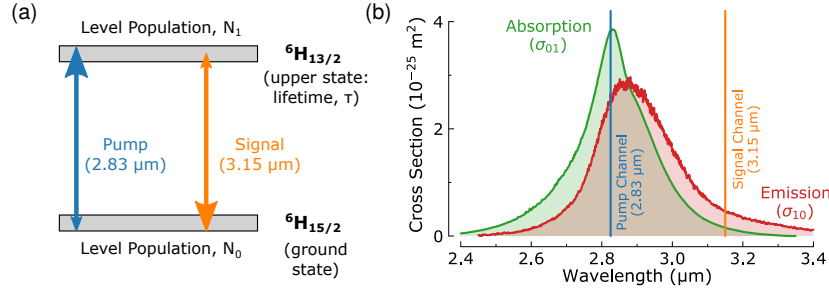


FIGURE 13.1 (a) Illustration of simple 2-level model for 3 μm Dy lasers. Arrows indicate the use of two optical channels to model the transfer of population between the levels (upward arrows indicate absorption; downward arrows indicate emission). The total fibre doping concentration is $N_{\text{doping}} = N_0 + N_1$. (b) Absorption and emission cross sections for Dy:ZBLAN.

not known, then repeated simulations could be performed with varying signal channel wavelengths to find the case with the lowest lasing threshold, which indicates the free-running wavelength.

Models can be made more accurate by including amplified spontaneous emission (ASE), which is implemented by adding a number of channels spanning the emission region with, for example, 10s nm width. Using more channels with narrower channel widths can increase accuracy, but at greater computational cost. Clearly there is a trade-off here and for many reported CW mid-IR fibre laser simulations, it is worth highlighting that good agreement is often found with experimental results by using only pump and signal channels, i.e. neglecting ASE.

Finally, it is important to note that optical channels are defined for a single propagation direction only, in order to include the effect of mirror reflectivities. Therefore, for each wavelength, two channels must be included in the model (which are coupled by cavity reflectivity boundary conditions, as described in Section 13.2.4). The power along the length of fibre at channel wavelength λ can thus be written as $P^+(\lambda, z)$ and $P^-(\lambda, z)$ at any given time t , where z is the longitudinal coordinate and $+$ and $-$ denote travelling direction along the fibre, e.g. from left to right and vice versa, respectively.

13.2.2 Basic 2-Level System Formulation

In the simplest laser rate equation system, only two energy levels—a ground state and an excited state—are involved in the model. Two optical transitions may appear between those two levels: an upward transition that is creating the excitation, and a downward transition that is emitting / amplifying light using that excitation. Additionally, any relaxation processes that result in a spontaneous decay of the excited state can be combined in the effective lifetime of the excited state τ .

For practical simulations, four optical channels can be considered: $P^+(\lambda_p, z)$ and $P^-(\lambda_p, z)$ for the pump radiation, and $P^+(\lambda_s, z)$ and $P^-(\lambda_s, z)$ for the laser signal. The evolution of the power in the laser channel can then be written as

$$\frac{dP^\pm(\lambda_s, z)}{dz} = \pm P^\pm(\lambda_s, z) [g(\lambda_s, z) - l_s] + P_{\text{spon}}(\lambda) \quad (13.1)$$

with the effective gain $g(\lambda_s, z)$, the background losses other than absorption l_s and $P_{\text{spon}}(\lambda_s)$ accounting for the spontaneous emission into the laser channel. Similarly the evolution in the pump channels can be written as

$$\frac{dP^\pm(\lambda_p, z)}{dz} = \pm P^\pm(\lambda_p, z) [g(\lambda_p, z) - l_p] + P_{\text{spon}}(\lambda) \quad (13.2)$$

with the effective absorption $\alpha(\lambda_p, z)$ and background losses l_p . Note that in both cases the absorption and emission for pump and signal are accounted for in their respective effective gain and absorption terms. These are as follows

$$g(\lambda_s, z) = \Gamma(\lambda_s) [\sigma_{10}(\lambda_s)N_1(z) - \sigma_{01}(\lambda_s)N_0(z)] \quad (13.3)$$

for signal gain and absorption, and

$$g(\lambda_p, z) = \Gamma(\lambda_p) [\sigma_{10}(\lambda_p)N_1(z) - \sigma_{01}(\lambda_p)N_0(z)] \quad (13.4)$$

for pump absorption, where $\Gamma(\lambda)$ are the mode overlap integrals with the doped fibre core, $\sigma_{10}(\lambda)$ are the emission and $\sigma_{01}(\lambda)$ are the absorption cross-sections at laser signal and pump wavelengths, as designated by the subscripts s and p, respectively. The atomic populations (or ionic populations, which is the technically more correct term) in the ground and excited states that interact with the optical transitions are described by their respective number densities $N_0(z)$ and $N_1(z)$. These enumerate how many of the ions per volume are found in the ground and the excited state at position z along the doped fibre core.

While the dominant power change from the gain medium will be reduction of pump power through absorption and enhancement of signal power through emission, it should be noted that Eqn. 13.3 and Eqn. 13.4 also account for emission of light into the pump channels and absorption of light from the signal channels. This is an important phenomena to include, particularly in the case of in-band pumped lasers where signal reabsorption can be strong.

The spontaneous emission can be expressed as

$$P_{\text{spon}}(\lambda) = n_{\text{modes}}\Gamma(\lambda)\sigma_{10}(\lambda)N_1(z)E_{\text{phot}}\Delta f \quad (13.5)$$

for each channel with photon energy $E_{\text{phot}} = hc/\lambda$ and channel spectral width Δf . The parameter n_{modes} is the number of guided transverse modes— $n_{\text{modes}} = 2$ for the typical case of a fibre supporting only the fundamental mode, which comprises two orthogonal polarisations [8]. This term is important when including

ASE channels but can be neglected when using only monochromatic pump and signal channels. Alternatively, as a simplified way to include spontaneous emission without introducing additional ASE channels, one could set the channel width for the signal channel here equal to the laser gain bandwidth (e.g. as used for modelling spontaneous emission-initiated pulsation in Ref. [6]).

The dynamics of the local excited state atomic population $N_1(z, t)$ at position z and time t can then be described by a rate equation, including terms which represent all the processes that either excite the ions (adding to the population, denoted by the + sign) or relax them (removing from the population, denoted by the – sign):

$$\begin{aligned} \frac{dN_1(z, t)}{dt} = & N_0(z, t) \left(\frac{\Gamma(\lambda_s)\sigma_{01}(\lambda_s)P(\lambda_s, z, t)}{A_{\text{core}} \times hc/\lambda_s} + \frac{\Gamma(\lambda_p)\sigma_{01}(\lambda_p)P(\lambda_p, z, t)}{A_{\text{core}} \times hc/\lambda_p} \right) - \\ & N_1(z, t) \left(\frac{\Gamma(\lambda_s)\sigma_{10}(\lambda_s)P(\lambda_s, z, t)}{A_{\text{core}} \times hc/\lambda_s} + \frac{\Gamma(\lambda_p)\sigma_{10}(\lambda_p)P(\lambda_p, z, t)}{A_{\text{core}} \times hc/\lambda_p} + \frac{1}{\tau} \right) \end{aligned} \quad (13.6)$$

where $P(\lambda_s, z, t) = [P^+(\lambda_s, z, t) + P^-(\lambda_s, z, t)]$ is the total laser signal power and $P(\lambda_p, z, t) = [P^+(\lambda_p, z, t) + P^-(\lambda_p, z, t)]$ is the total pump power at position z and time t , A_{core} is the fibre core area, h is the Planck constant, c is the speed of light in vacuum and τ is the effective lifetime of the excited state. Sometimes a relaxation rate R is used which is the inverse of the lifetime, i.e. $R = 1/\tau$, and that total rate is a sum of all the partial rates of transitions that are proportional to the population density N_1 , such as e.g. fluorescence (radiative) and multiphonon (non-radiative) processes, but excluding the stimulated emission.

The total number of ions $N_{\text{doping}} = N_0 + N_1$ is always conserved. Since there are only two levels involved in this case, the ground level population differential equation is simply

$$\frac{dN_0(z, t)}{dt} = -\frac{dN_1(z, t)}{dt}. \quad (13.7)$$

Due to the local electric field in the glass host material, a rare earth ion's energy manifold can be split into several *Stark levels*. For many practical cases, however, those Stark levels can be counted together as one *level* in the rate equation model because of the rapid thermalisation among them. This is taken into account with the *effective cross sections* for absorption and emission that each results from the contributions and temperature-dependent distributions of individual Stark levels. Further discussion on how to obtain the required cross sections and overlap integrals is presented in Sec. 13.2.5.

Equations 13.1–13.6 form the rate equations system and describe the full evolution of the power and level populations in both space and time for a simple two-level system.

13.2.3 Matrix Formulation

The laser rate equations that were introduced in the previous section involved only two atomic energy levels and a small number of optical transitions between them. Many active ions in the mid-IR, however, involve substantially more complex energy level structures and a larger number of transitions among them. In this section, we show how to formulate such a complex rate equation system of equations in matrix notation, which is not only elegant in form but also enables application of efficient algorithms for solving this numerically.

The power evolution $P(\lambda, z)$ for each spectral channel of wavelength λ along the fibre can be written as:

$$\frac{dP^\pm(\lambda, z)}{dz} = \pm \left(P^\pm(\lambda, z) \left(\Gamma(\lambda) \left[\sum_{i,j} \sigma_{ij}(\lambda) N_i(z) - \sigma_{ji}(\lambda) N_j(z) \right] - l(\lambda) \right) + P_{\text{spon}}(\lambda) \right) \quad (13.8)$$

where $\Gamma(\lambda)$ is the core overlap factor and $l(\lambda)$ is the background loss of each individual spectral channel. Each atomic energy level is assigned a numerical label, where the ground level is 0 (with population N_0), the first excited state is 1 (with population N_1), the second excited state is 2 (with population N_2) etc. The total number of levels included in the model is m . The σ_{ij} term is the cross section of the transition between $i \rightarrow j$ levels. When $i < j$ this denotes absorption and when $i > j$ it denotes emission. The summation term is taken over all combinations of levels pairs ($i, j \neq i$), to account for all possible transitions between energy levels, which includes up to $m \times (m - 1)$ possible terms.

The spontaneous emission $P_{\text{spon}}(\lambda, z)$ term can then be written as:

$$P_{\text{spon}}(\lambda, z) = n_{\text{modes}} \Gamma(\lambda) \left(\sum_{\substack{i,j \\ i>j}} \sigma_{ij}(\lambda) N_i(z) \right) \frac{hc\Delta f}{\lambda}. \quad (13.9)$$

Only downward transitions contribute, associated with their respective radiative relaxations between levels $i \rightarrow j$ where $i > j$.

The atomic level populations for all m levels are written in a vector $\mathbf{N} = [N_0, N_1 \dots N_{m-1}]$, and their respective rate equations can then be expressed at time t and position z in matrix notation as:

$$\frac{d\mathbf{N}}{dt} = \mathbf{L}\mathbf{N} + \mathbf{W}. \quad (13.10)$$

where \mathbf{L} and \mathbf{W} are matrices which describe the linear and nonlinear population change rate terms, respectively. The linear matrix includes spontaneous emission, stimulated absorption/emission and multiphonon relaxation terms,

represented in the form:

$$\mathbf{L} = \begin{bmatrix} -\sum_{i=0}^{m-1} R_{0i} & \cdots & R_{(m-1)0} \\ \vdots & \ddots & \vdots \\ R_{0(m-1)} & \cdots & -\sum_{i=0}^{m-1} R_{(m-1)i} \end{bmatrix}. \quad (13.11)$$

Note that subscript $m - 1$ refers to the highest energy level in the model, since the first level is assigned the index 0. The non-diagonal elements on the right hand side represent the incoming (positive) rates of changes to the population N_i from all the individual levels $j \neq i$. The diagonal elements contain the sum of all the outgoing (thus negative) rates. These individual rates are:

$$R_{ij} = \beta_{ij}/\tau_i + R_{ij}^{\text{nr}} + \sum_{\lambda} \sigma_{ij}(\lambda) \frac{P(\lambda)\Gamma(\lambda)}{A_{\text{core}} \times hc/\lambda} \quad (13.12)$$

where τ_i is the radiative lifetime β_{ij} is the associated branching ratio, R_{ij}^{nr} is the non-radiative relaxation rate, and the third term represents the stimulated absorption/emission for the $i \rightarrow j$ transition, summed over all spectral channels (in both propagation directions, $P(\lambda) = P^+(\lambda) + P^-(\lambda)$).

The nonlinear matrix describes changes in level populations due to the energy transfer processes (energy transfer upconversion (ETU), cross relaxation etc.), which can be written as:

$$\mathbf{W} = \begin{bmatrix} \sum_{k=0 \text{ or } l=0}^{i,j,k,l} w_{ijkl} N_i N_j - \sum_{i=0 \text{ or } j=0}^{i,j,k,l} w_{ijkl} N_i N_j \\ \vdots \\ \sum_{k=(m-1) \text{ or } l=(m-1)}^{i,j,k,l} w_{ijkl} N_i N_j - \sum_{i=(m-1) \text{ or } j=(m-1)}^{i,j,k,l} w_{ijkl} N_i N_j \end{bmatrix} \quad (13.13)$$

where the energy transfer coefficient w_{ijkl} denotes the changing population states of the first ion $i \rightarrow k$ and the second ion $j \rightarrow l$ for a particular interionic process. The terms of this matrix include products of two population values, making the rate equation nonlinear.

13.2.4 Boundary Conditions

Having formulated a system of equations for the photonic and atomic populations along a doped fibre, the only remaining physical phenomena to add into the model is the behaviour of light at the ends of the fibre. This could include reflections from mirrors, which couple power from forwards-travelling wavelength channels into backwards-travelling channels (and vice versa) according to some wavelength-dependent reflectivity value. The unreflected quantity of light can then be taken as the output from the laser. Additionally, optical inputs to the

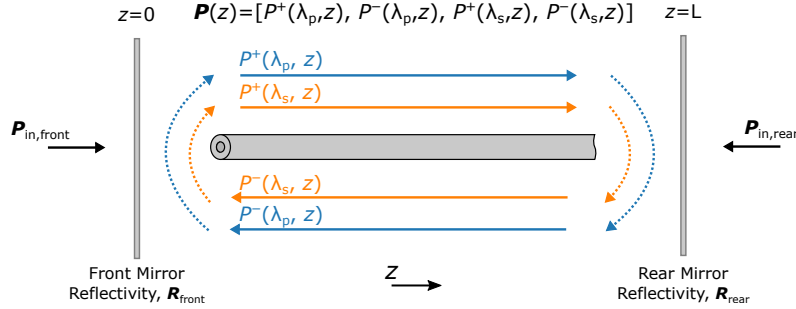


FIGURE 13.2 Illustration of optical channels (for both forwards (+) and backwards (−) directions) and cavity parameters for a simulation including 2 wavelengths.

fibre such as pump power (and possibly signal power for amplifier modelling) are accounted for at these facets (illustrated in Fig. 13.2).

These inputs and reflectivities are the boundary conditions of the power flow equation (Eqn. 13.8). At the distal fibre end ($z = L$), these can be expressed as:

$$P^-(z = L, \lambda) = R_{\text{rear}}(\lambda)P^+(z = L, \lambda) + (1 - R_{\text{rear}}(\lambda))P_{\text{in, rear}}(\lambda) \quad (13.14)$$

where $R_{\text{rear}}(\lambda)$ is the reflectivity at wavelength λ for the rear-end mirror and $P_{\text{in, rear}}(\lambda)$ is the power at wavelength λ injected backwards into the fibre at the rear end. Similarly, at the front fibre facet ($z = 0$):

$$P^+(z = 0, \lambda) = R_{\text{front}}(\lambda)P^-(z = 0, \lambda) + (1 - R_{\text{front}}(\lambda))P_{\text{in, front}}(\lambda) \quad (13.15)$$

where the ‘front’ subscripts imply the same quantities as above, but at the front fibre tip.

Using the matrix formalism, it is natural to handle the power of each optical channel as a vector. For example, for the case of one pump and one signal wavelength, one could define $\mathbf{P}(z) = [P^+(\lambda_p, z), P^-(\lambda_p, z), P^+(\lambda_s, z), P^-(\lambda_s, z)]$. Other channel properties such as reflectivities, overlap factors and background loss can also be stored as vectors and multidimensional matrices can hold the cross section values for all optical channels for all possible transitions. With such data structures, many of the equations in this section can be computed using efficient parallel matrix operations, rather than iterating over all wavelengths and transitions sequentially. Note that \mathbf{P} and \mathbf{N} are also functions of time, even though this t variable was not explicitly included above for brevity of notation—therefore pulse pumping / cavity modulation can be modelled by making the boundary conditions time-varying too.

13.2.5 Preparation of Numerical Spectroscopic Data

To obtain meaningful performance predictions from simulations, it is critical to provide accurate spectroscopic inputs to the model. We therefore briefly

consider how to acquire efficient numerical representations of the relevant data.

13.2.5.1 Cross Sections

Absorption and emission cross sections are required for all relevant transitions (i.e. transitions with non-zero cross section at the wavelengths of interest). These are typically obtained from direct measurements of the absorption or fluorescence spectra of rare-earth-doped materials (e.g. processed using the Füchtbauer–Ladenburg equation and taking the doping concentration into account) [7]. Alternatively, if only one of the two cross sections is available, the other can be computed using the McCumber relations.

While a simulation could take individual value inputs for the cross section at each optical channel wavelength, it is far more flexible to incorporate the full spectral profile for each cross section into the model. For example, the original measurement data file could be loaded each time and interpolated for the user-specified wavelength channels. However, a more efficient and widely used numerical representation is to fit a summation of n Gaussians to the raw data (e.g. using a least-squares fitting routine):

$$\sigma(\lambda) = \sum_{i=0}^n A_i \exp\left(-\frac{(\lambda - \lambda_i)^2}{2w^2}\right) \quad (13.16)$$

where A_i , λ_i and w_i are the amplitude, central position, and width, respectively, for the i^{th} fitted Gaussian. The number of Gaussian required, n depends on the complexity of the spectral shape, which may be determined empirically. As a result, only a small number of fitting coefficients need to be stored to accurately describe the full cross section profile. Figure 13.3 demonstrates the application of this technique to the Dy:ZBLAN ${}^6\text{H}_{15/2}$ — ${}^6\text{H}_{13/2}$ transitions, showing excellent fits using only 3 Gaussians.

It should be noted that we technically work with *effective* cross sections for modelling. By rigorous definition, a transition cross section is defined between exact electronic levels, which for rare-earth-doped fibres means considering each individual Stark-split sublevel within each manifold. Stark-split levels are closely spaced, however and are thermally coupled (with relative occupancy described by the Boltzmann distribution, assuming rapid thermalisation within manifolds). Therefore, when absorption / fluorescence spectra are measured at room temperature then processed to compute the effective cross sections, these spectra intrinsically include the effects of thermal occupancy of the Stark levels and the numerous possible transitions between all sublevels [10]. Hence, for practical modelling, cross sections are simply defined for manifold to manifold transitions.

13.2.5.2 Radiative Lifetimes and Branching Ratios

Beyond quantifying the spectral shape of transitions, it is important to determine the general radiative behaviour for each manifold, in order to compute

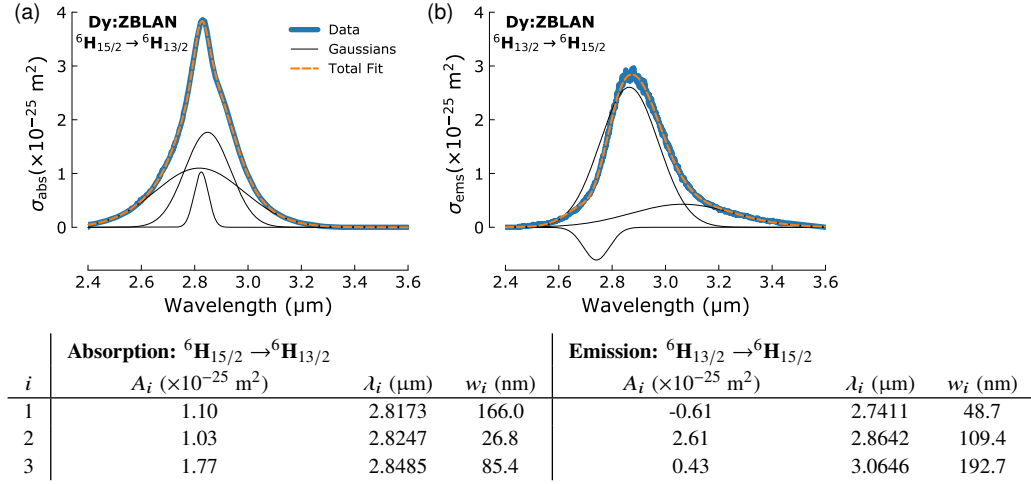


FIGURE 13.3 (a) Absorption and (b) emission cross sections for Dy:ZBLAN ${}^6\text{H}_{15/2} \rightarrow {}^6\text{H}_{13/2}$ transition, showing sum of Gaussians fitting and tabulated fitting parameters.

the radiative lifetime and branching ratios. This would be an impractical task experimentally for ions where many level are considered. Fortunately, however, Judd-Ofelt theory offers a simple solution for estimating oscillator strengths of all $4f-4f$ transitions for a lanthanide ion in a given host, using only 3 experimentally fitted parameters, Ω_2 , Ω_4 and Ω_6 . For Judd-Ofelt calculations, tables of reduced matrix elements of quantum mechanical tensor operators for each gain medium are also required as inputs, but for a given rare-earth ion, these values are essentially host-invariant and it has become standard to use readily available tabulated values of matrix elements for rare-earths in LaF_3 [12] (for a detailed explanation how these are originally computed from fundamental quantum mechanics, see Ref. [13]).

A more comprehensive treatment of Judd-Ofelt theory is presented in earlier chapters of the book. For practical modelling, one can also often find computed radiative lifetimes and branching ratios in the literature for the doped gain medium of interest.

13.2.5.3 Nonradiative Lifetimes

Unlike spontaneous *radiative* decay (where the population of each manifold feeds into all lower-energy manifolds in a ratio given by the branching ratio), for the spontaneous *nonradiative* (i.e. multiphonon-induced) decay, the population decays only into the next-lowest energy level. In practice, measurements of manifold lifetimes (e.g. using fluorescence temporal decay measurements) cannot resolve the relative contributions from radiative and nonradiative phenomena; the total measured lifetime is the inverse sum of the inverse radiative

(τ_r) and nonradiative (τ_{nr}) lifetimes: $1/\tau = 1/\tau_r + 1/\tau_{nr}$. For mid-IR transitions (typically between closely spaced levels), nonradiative lifetimes are often much shorter than radiative lifetimes. In this case, one could approximate the nonradiative lifetime as being equal to the total measured lifetime in the model for simplicity.

Alternatively, it is also possible to estimate the nonradiative lifetime by calculating the nonradiative decay rate R^{nr} , where $R^{nr} = 1/\tau_{nr}$, through an empirically derived ‘energy-gap law’ [14]. For a transition between levels of energy spacing ΔE , in a host with maximum phonon energy E_{phonon} , the number of phonons for a multiphonon decay is: $p = \Delta E/E_{\text{phonon}}$. The nonradiative relaxation rate at temperature T is then given by:

$$R^{nr} = B[n(T) + 1]^p \exp(-\alpha \Delta E) \quad (13.17)$$

where B and α are host-dependent parameters and $n(T)$ is the Bose-Einstein occupation number. For ZBLAN, one can use $B = 1.59 \times 10^{10} \text{ s}^{-1}$, $\alpha = 5.19 \times 10^{-3} \text{ cm}$ and $E_{\text{phonon}} = 500 \text{ cm}^{-1}$, taken from tabulated values in Ref. [14].

13.2.5.4 Energy Transfer Coefficients

Finally, for highly doped fibres, we must consider the possibility of energy transfer between dopant ions (e.g. cross relaxation, ETU, etc., which occur due to dipole-dipole resonant interactions). Such energy transfer can be between ions of the same type, or between different species of ion if the fibre is co-doped. These phenomena can be usefully exploited, e.g. to depopulate the lower-laser-level for $3 \mu\text{m}$ lasing in Ho/Pr:ZBLAN, or may act against the desired laser transition. Unfortunately, this is often the most challenging parameter to determine for a model and depends critically on the doping concentration.

The cross sections and radiative properties we previously discussed for simulating gain media are effectively independent of doping concentration. This simplifies the acquisition of modelling parameters, since a wide number of studies have already been published that offer such data and when optimizing laser designs, the dopant concentration can be freely varied by the user. Energy transfer coefficients, however, directly depend on doping concentration, since the strength of dipole-dipole interactions is related to the distance between ions—increased doping thus leads to greater transfer coefficients. It is also possible for phonons to be involved in these dynamics, known as phonon-assisted energy transfer.

These parameters can be inferred from experimental measurements, typically using bulk glass samples in complex pump-probe experiments, that require knowledge of all other parameters that are involved in transitions from the same level(s). This may lead to large uncertainties and the resulting values are only strictly valid for gain media of the same doping concentration. A small number of studies using batches of samples with varying concentrations have proposed various empirical relations to describe how coefficients vary with concentration,

which could be incorporated into the rate equation to allow the user to vary the doping concentration while still including energy transfer effects. Energy transfer parameters turn out to be critical to the operation of mid-IR Er fibre lasers, and they are the subject of more in-depth discussion in our case studies in Sec. 13.2.10.

13.2.5.5 Fibre Mode Properties

The final input parameters to be discussed are the attenuation per length $l(\lambda)$ and modal overlap $\Gamma(\lambda)$, which are properties of the gain fibre geometry / fabrication quality, rather than the ion spectroscopy. Fibre attenuation (i.e. background loss) arises from absorption and scattering effects, both from the intrinsic host glass and additional impurities added during the fabrication process. While doped silica fibres can be produced with less than 0.2 dB/km loss, state-of-the-art ZBLAN fibre manufacturing typically results in doped fibres with 0.1–0.5 dB/m attenuation. For optimum accuracy in modelling, the loss spectrum should be measured (this can be heavily wavelength dependent, e.g. due to water absorption peaks), then the loss value at each spectral channel used in the model can be found by interpolation. However, it can be practically difficult to isolate background loss from measurements of white-light transmission through fibre if the dopant absorbs strongly in the region of interest. Thus, in practice, a constant background loss value (independent of channel wavelength) is often used.

The second parameter, modal overlap $\Gamma(\lambda)$, refers to the overlap integral of guided optical modes with the doped fibre core. For a fully rigorous analysis, one should include the radial dependence of power in the rate equations since the mode intensity varies across the fibre diameter. However, a widely used approximation which has minimal reduction in accuracy for step-index-geometry fibres is to assume the mode intensity is constant (i.e. a flat-top beam) and apply an overlap factor to account for the reduction in optical interaction with the dopant due to the mode field extending beyond the doped core region [8]. For single-mode step-index fibres with known core diameter and numerical aperture (NA), $\Gamma(\lambda)$ can be computed by performing an eigenmode analysis for a cylindrical step-index waveguide geometry (discussed in Section 13.4.1). The outcome of this analysis is the mode-field diameter $w(\lambda)$ for each wavelength in the fibre, which can be combined with the fixed-size core diameter d to compute the overlap integral factor [15]:

$$\Gamma(\lambda) = 1 - \exp\left(\frac{-2d^2}{w(\lambda)^2}\right). \quad (13.18)$$

Note that each wavelength has a different overlap factor, thus this can be a vector-type input to the model if using the matrix formalism. For single-clad fibres, one often finds $\Gamma \sim 0.6$ – 1.0 . For example, for a 12.5 μm core diameter fibre with 0.16 NA (that gives single-mode cut-off at 2.6 μm), the Marcuse equation predicts a mode-field diameter of 15.2 μm at 3 μm wavelength, yielding $\Gamma = 0.74$.

Thus far we have considered single-mode single-clad fibres where both pump and signal modes are core-guided. However, our model can be simply adapted to double-clad fibres by re-defining $\Gamma(\lambda)$ where $\lambda = \lambda_p$. As light guided by the cladding is multimoded and covers a wide area, to account for this effect (assuming uniform pump intensity across the whole area), one can set Γ as the ratio of the geometric core area to the inner cladding area for pump wavelengths that are coupled into the inner cladding:

$$\Gamma(\lambda) = \frac{\pi(d/2)^2}{\pi(d_{\text{clad}}/2)^2} \quad (13.19)$$

where d_{clad} is the *effective* inner cladding diameter (this assumes the generated signal is confined to the core, which is reasonable since typically only the core region is doped). Note that double-clad fibres typically employ a non-circular cladding, thus the *effective* cladding diameter may be smaller than actual cladding diameter [3], requiring empirical adjustment of d_{clad} within a reasonable window of uncertainty to optimize agreement between simulations and the experiment. Indeed, it should be noted that many of the input parameters for simulations will have an associated uncertainty range. Therefore, a valuable step in developing a robust numerical model is to compare simulations to trusted experimental data sets, adjusting numerical parameters within uncertainty bounds to effectively ‘calibrate’ the model to the experiment.

13.2.6 Steady State Solutions: Modelling CW Systems

The primary aim of fibre laser/amplifier modelling is to find the evolution of optical power along the fibre for all wavelength channels, $P(\lambda, z, t)$. Once solved, the power emitted by the cavity at either end can be obtained after correcting for the mirror transmission: e.g. power out the distal fibre end: $P_{\text{out, rear}}(\lambda, t) = P^+(\lambda, z = L, t) (1 - R_{\text{rear}}(\lambda))$. This requires Eqns. 13.8 and 13.10 to be solved, subject to boundary conditions (which correspond to mirror reflectivities and injected powers), as formulated earlier in this chapter. While analytical solutions may not exist, numerical methods can be used, which require the equations to be discretised in both space and time. We begin by considering steady-state solutions (i.e. simulating CW lasers), which permits us to ignore the temporal evolution and consider only the stabilised solution after a long time period by setting $d\mathbf{N}/dt = 0$. We thus need to solve $\frac{d\mathbf{P}}{dz}$ for all wavelength channels simultaneously, where the fibre length L is divided up into M discrete segments of size $\Delta z = L/M$. Fig. 13.4 illustrates the discretisation approach for our problem.

Finding the power at each point in the fibre is a two-part problem. Firstly, the power flow equation $\frac{d\mathbf{P}}{dz}$ with boundary conditions is a two-point boundary value problem (BVP). Secondly, this BVP equation depends on the population densities $\mathbf{N}(z, t)$, which are not known, but are defined by the atomic population equation $\frac{d\mathbf{N}}{dt}$ at each position along the fibre.

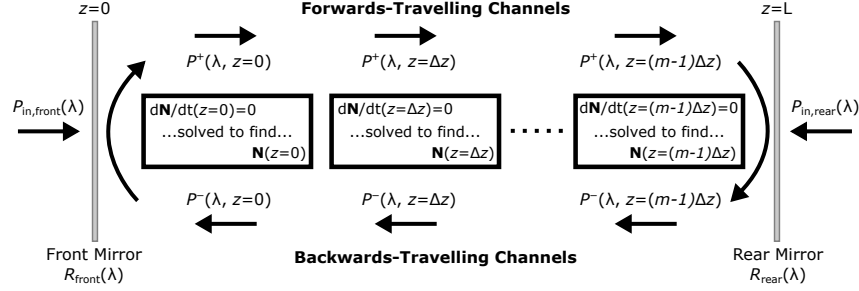


FIGURE 13.4 Illustration of numerical solution approach where the fibre length is discretised into m equal length samples.

13.2.6.1 Solving Rate Equations

We first consider how to solve $\frac{d\mathbf{N}}{dt} = 0$ to find \mathbf{N} , the vector of population densities for all relevant m levels of the ion in a single length segment. This process is repeated for each z segment. In the matrix formalism, Eqn. 13.10 showed that this equation has the form:

$$\frac{d\mathbf{N}}{dt} = \mathbf{L}\mathbf{N} + \mathbf{W} \quad (13.20)$$

where \mathbf{L} is a matrix comprising linear population change rate terms and \mathbf{W} is a matrix of nonlinear terms.

If energy transfer coefficients are not included for a simulation ($\mathbf{W} = 0$), this will be a system of *linear* equations, where $\frac{d\mathbf{N}}{dt}$ is a column vector of 0s. Note that to ensure a well-determined matrix equation (i.e. avoiding a singular matrix for \mathbf{L}), one of the \mathbf{L} matrix rows and a value in the $\frac{d\mathbf{N}}{dt}$ vector should be set to enforce the known condition: $N_0 + N_1 + \dots + N_{m-1} = N_{\text{doping}}$. Exact solutions can then be found by inverting the \mathbf{L} matrix: $\mathbf{N} = \mathbf{L}^{-1} \frac{d\mathbf{N}}{dt}$. Fast and efficient numerical recipes are well-known for solving such linear equations [16], and are readily available in high-level programming languages like Python and MATLAB.

If the simulation includes energy transfer coefficients, however, the system of equations contains nonlinear terms ($\mathbf{W} \neq 0$), preventing simple matrix inversion-based solving strategies and hindering determination of the exact solution. In this case, the problem can be approached using root finding algorithms to estimate the solution to reasonable precision. Such algorithms are also readily available in common programming tools, although executions times are significantly increased compared to solving linear equations. For any discrete segment of the fibre, we have now described how to compute the local population levels subject to known power values at that fibre position.

13.2.6.2 Solving Power Flow Equations

Returning to consider the power flow equation, we note that this is a difficult problem since we need to find the power values for multiple wavelengths at each position in the fibre, such that all values satisfy $\frac{dP}{dz}$ subject to boundary constraints at each end. Fortunately, this class of two-point BVP appears in many physical problems and a number of numerical methods exist to approximate the solutions.

In the field of laser modelling, traditionally, the most commonly used family of numerical methods have been *shooting methods* and *relaxation methods*. For shooting-based techniques, the unknown power values at one end of the fibre are estimated, then propagated along the fibre according to $\frac{dP}{dz}$ and compared to the known values for each channel at the other end (e.g. this could involve guessing the residual pump power for a counter-pumped amplifier, then comparing the computed pump power at the pump input side to the true pump input). Based on this comparison, the input estimations are updated and the processes is repeated until a self-consistent solution is found. A similar iterative approach concerns relaxation methods, where an estimated solution is propagated back and forth along the fibre until it convergences to a steady self-consistent state. One of the greatest challenges with these techniques, and indeed all numerical modelling of this form, is reliably obtaining convergence (i.e. avoiding simulations which run forever without solution). Additionally, for practical usage, obtaining convergence in a reasonable time frame is also important. The initial guess solution (the ‘seed’) provided to the solver, is therefore critically important: the nearer the guess is to the actual solution, the faster the simulation will converge on that solution.

On a practical level, however, we note that most modern high-level programming languages include libraries with functionality for efficiently solving such problems, making use of other optimized mathematical methods and with the aim of broad applicability to a large class of problems. For example, Python’s NumPy library and MATLAB provide `solve_bvp` and `bvp4c`, respectively, which can solve a system of equations input as a matrix alongside the boundary conditions to some desired tolerance of solution (based on finite-difference collocation methods [17]). Therefore, the optimum solution strategy will depend on the programming language in which the problem is implemented.

There are also many solving algorithm parameters that can be chosen for optimum numerical differential equation solving. Firstly, the discretisation of fibre length is important: if too many steps are taken, the solver will be unnecessarily slow, whereas too few will compromise the accuracy of the solution. Practically, one can find suitable discretisation by adjusting the number of segments until the simulation output becomes independent of further increase in segment count (i.e. confirming the grid-invariance of the simulation).

Secondly, for some of the above described methods, an initial guess ‘seed’ solution must be provided—which should be as close to the solution as possible. If the seed is far from the true solution, even optimized solvers may not succeed.

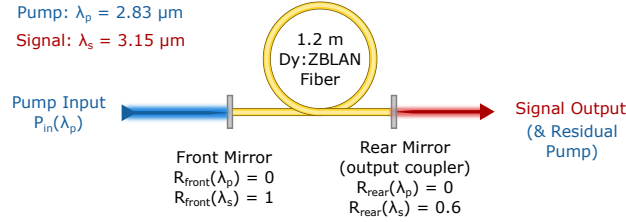


FIGURE 13.5 Dy:ZBLAN CW laser cavity schematic.

As a simple approach, one can choose constant seed powers at some reasonable level based on the inputs. However, an improved seeding ‘guess solution’ can be offered using knowledge of laser physics, thus maximizing the opportunity for the solver to quickly converge to the solution. For example, this could include estimating the pump as following small-signal absorption for the given fibre (of course, in practice, saturation effects change this, but it provides a good first guess). Even if a single method does not converge for every simulation input, these can be manipulated empirically to optimize convergence. The ‘stiffness’ of the set of differential equations to be solved will also vary between laser transitions of interest, thus the optimum choice of numerical algorithm and its parameters depends on the exact problem specification.

13.2.7 Case Study: In-Band-Pumped Single-Clad CW Dy:ZBLAN Fibre Laser

To illustrate the insight gained in the laser design process and performance predictions that can be achieved using simulations, we now present a case study for a Dy-doped ZBLAN fibre laser. Dy is emerging as a promising rare-earth ion for mid-IR technology, partly as it offers a spectroscopically simple transition between the first excited state and ground state for 3 μm emission. This can be in-band pumped at 2.8 μm and at these wavelengths, there are no known ESA or energy-transfer effects, avoiding the need for dual-wavelength pumping or co-doping to achieve efficient lasing.

First, we consider a simple linear cavity comprising 1.2 m single-clad Dy:ZBLAN fibre with $N_{\text{doping}} = 3.66 \times 10^{25} \text{ m}^{-3}$ (0.2 mol%), 12.5 μm core diameter and 0.16 NA (yielding 2.6 μm single-mode cut-off wavelength). Mirrors are included at the fibre ends with a narrow reflection band (i.e. FBGs) at 3.15 μm . Pump light at 2.83 μm is injected at the input through the front mirror, which has 0% reflectivity at the pump wavelength and 100% reflectivity for the signal wavelength. The rear-mirror is also transparent for the pump, but is 60% reflective for the signal, thus acting as the output coupler. Such a laser design is similar to experiments reported in Ref. [18]. Table 13.1 summarises the model parameters.

TABLE 13.1 Modelling parameters for the CW Dy:ZBLAN fibre laser

Parameter	Symbol	Value
Radiative lifetime	$\tau_{r,1}$	48.6 ms
Branching ratio	β_{10}	1
Non-radiative lifetime	$\tau_{nr,1}$	650 μ s
Doping concentration	N_{doping}	$3.66 \times 10^{25} \text{ m}^{-3}$
Fibre background loss	l	0.2 dB m^{-1}
Pump wavelength	λ_p	2.83 μ m
Pump absorption cross section	$\sigma_{01}(\lambda_p)$	$3.83 \times 10^{-25} \text{ m}^{-3}$
Pump emission cross section	$\sigma_{10}(\lambda_p)$	$2.58 \times 10^{-25} \text{ m}^{-3}$
Pump overlap factor	$\Gamma(\lambda_p)$	0.79
Signal wavelength	λ_s	3.10 μ m
Signal absorption cross section	$\sigma_{01}(\lambda_s)$	$2.8 \times 10^{-26} \text{ m}^{-3}$
Signal emission cross section	$\sigma_{10}(\lambda_s)$	$6.8 \times 10^{-26} \text{ m}^{-3}$
Signal overlap factor	$\Gamma(\lambda_s)$	0.74
Front mirror: pump reflectivity	$R_{\text{front}}(\lambda_p)$	0
Front mirror: signal reflectivity	$R_{\text{front}}(\lambda_s)$	1
Rear mirror: pump reflectivity	$R_{\text{rear}}(\lambda_p)$	0
Rear mirror: signal reflectivity	$R_{\text{rear}}(\lambda_s)$	0.6

To simulate this system, which is outlined in Fig. 13.5, only two wavelengths need to be included in the model: a pump ($\lambda_p = 2.83 \mu\text{m}$) and a signal ($\lambda_s = 3.15 \mu\text{m}$), resulting in four optical channels in the model, when accounting for both forwards and backwards propagating directions, as discussed in Section 13.2.1. For simplicity, monochromatic channels are assumed, with width $\Delta f = 0$, thus neglecting spontaneous emission. The input pump power is set to 1.6 W, which alongside the mirror reflectivities defines the boundary conditions. The simulation is executed by numerically solving the power flow equation as described above, using $M = 25$ segments to discretise the $L = 1.2$ m fibre length. Fig. 13.6(a) plots the results, showing the forwards- and backwards-travelling power evolutions. The forwards-travelling pump power $P^+(\lambda_p)$ injected at $z = 0$ is seen to steadily decay along the fibre due to ground-state absorption (GSA). Since both front and back mirrors have 0 reflectivity for the pump channel, no power is coupled into the backwards pump channel $P^-(\lambda_p)$.

In practice, the 3.15 μm signal power would have grown from spontaneous emission over many round-trips. Here, by solving for $dN/dt = 0$, we find the steady-state CW results and ignore the temporal evolution. We observe that the forwards-travelling intracavity signal power $P^+(\lambda_s)$ increases with distance from 1.89 W to 2.44 W, due to gain from the pumped Dy fibre. At the rear end ($z = 1.2$ m) the 60% reflective mirror extracts 0.97 W as the output power and the remaining light (1.47 W intracavity power) is reflected into the backwards-travelling signal channel $P^-(\lambda_s)$. Backwards travelling 3.15 μm light is amplified on the return trip, increasing to 1.89 W at $z = 0$, thus forming a self-consistent solution. The rate equation solutions also enable the inversion along the fibre

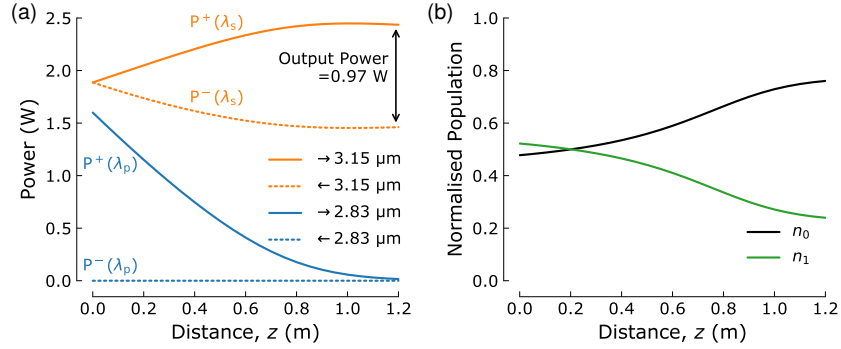


FIGURE 13.6 Dy:ZBLAN laser simulation results: variation of (a) optical power and (b) normalised level populations (i.e. $n_0 = N_0/N_{\text{doping}}$) with distance along the fibre.

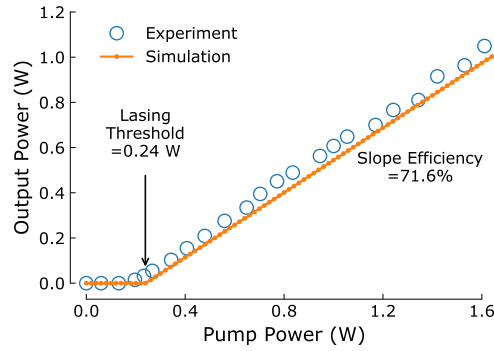


FIGURE 13.7 Comparison of laser output power at 3.15 μm for simulations and equivalent experiments (after [18]). Annotations shows the simulated threshold and slope efficiency values.

to be plotted [Fig. 13.6(b), normalised such that $n_i = N_i/N_{\text{doping}}$], thus offering insight beyond what could be practically measured. As expected, we see the strongest inversion near the pumped end.

Additional performance metrics can be obtained by recording the output power for repeated simulations with varying input parameters. For example, Fig. 13.7 shows the laser output power as a function of input power (each simulation data point corresponds to a different set of boundary conditions and complete execution of the numerical solver). The simulation shows clear laser behaviour, with a threshold at 0.24 W, followed by linear increase in power yielding a slope efficiency of 71.6%. This laser was also physically constructed [18], with component values matched to the simulation, and good agreement was found between experimental and simulated data over the range of input powers. The small deviation between the values could be related to

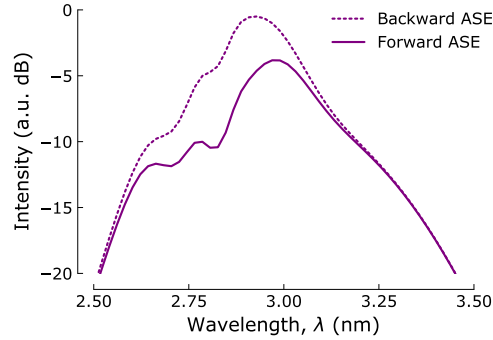


FIGURE 13.8 Simulated spectra (using numerical ASE channels with 20-nm width) for forwards-travelling ASE at the rear end of the fibre and backwards-travelling ASE at the front end.

laboratory measurement/component value uncertainties or to the fact that Dy-doped ZBLAN is a composite glass and thus the exact experimental composition may have varied slightly from the literature studies where spectroscopic data was obtained.

To extend the model, ASE can be included. In this case, we define numerous additional channels from 2.5–3.5 μm , spaced by 20 nm. The mirror reflectivity is set as 0 for all ASE channels. Repeating simulations with ASE showed negligible change in laser behaviour here, as expected since stimulated emission should dominate in a well-designed laser. However, ASE can strongly influence laser behaviour when this is not the case. Additionally, the inclusion of ASE channels in the model enables the ASE spectrum to be resolved. For example, Fig. 13.8 shows the output ASE spectra at the front and rear end of the fibre for this simulated setup.

It is interesting to note similar output ASE profiles at longer wavelengths ($> 3 \mu\text{m}$), but much stronger backwards travelling ASE at shorter wavelengths. This can be explained by noting the quasi-four-level nature of the 3 μm Dy transition and the variation in inversion with length [Fig. 13.6(b)]: at the rear end of the fibre, the inversion is reduced so there is stronger GSA, which attenuates ASE that overlaps the absorption band before it reaches the distal end. For ASE generated at the rear end of the fibre which travels backwards, however, this effect is less marked since the inversion is stronger ($> 50\%$, thus re-absorption is weaker) near the front facet. This illustrates how numerical modelling can provide significant insight not only in predicting performance, but in explaining observations.

From a laser design point of view, simulations can answer questions pertaining to optimum parameters for a given output specification. For example: what is the optimum fibre length and mirror reflectivity for efficient high-power emission? Fig. 13.9 shows the result of repeating the above modelling approach with

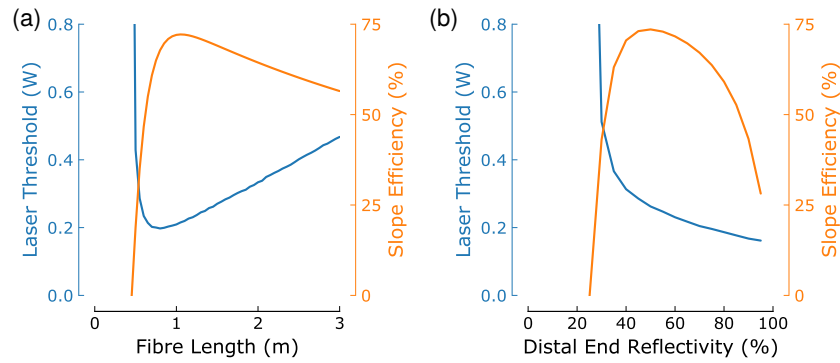


FIGURE 13.9 (a) Simulated laser threshold and slope efficiency as a function of: (a) doped fibre length; (b) reflectivity of the rear mirror (the output coupling ratio is 100% minus this value).

various fibre lengths and mirror reflectivities. In terms of fibre length, minimum thresholds of <0.3 W pump power occur for lengths around 1 m. Increasing length is seen to have a detrimental effect, due to both increased loss (doped ZBLAN fibre has relatively high background loss) and signal re-absorption. These effects also reduce the efficiency, thus optimum slope efficiencies exceeding 70% also occur around 1 m fibre length.

Further interesting effects are seen for performance variation with rear mirror signal reflectivity. Optimum efficiency is achieved for 40–60% reflectivities. For lower reflectivities, there is less stimulated emission due to reduced feedback, which leads to reduced pump absorption. As the pump is less utilised, the efficiency is reduced. At first glance, however, it may seem counter-intuitive that the efficiency also reduces for increasing reflectivities above 60%. This is due to the relatively high background loss: higher mirror reflectivities increase the cavity Q-factor, which increase the average number of cavity round-trips for a photon before it is emitted. While in doped silica fibre, the loss is sufficiently low that this does not affect the efficiency, with the 0.2 dB/m loss of doped ZBLAN fibre, the increased cavity lifetime leads to a longer effective time experiencing loss and thus, reduced laser efficiency. (This explanation was also verified by repeating simulations with zero loss, noting that efficiency remained constant around 70% for reflectivities above 50% in this case). Despite the lower slope efficiency, increasing reflectivities do always lead to a reduced laser threshold.

Finally, we consider the influence of laser wavelength on performance by changing the signal channel wavelength for which the narrow-band rear end mirror is 60% reflective. Fig. 13.10(a) shows the resulting output power from repeating numerous simulations with different signal wavelengths: watt-level emission is achieved from 2.85–3.3 μm . Outside of this range the output rapidly reduces to zero: due to approaching the in-band pump wavelength on the short wavelength edge and due to the low emission cross section (and thus, reduced

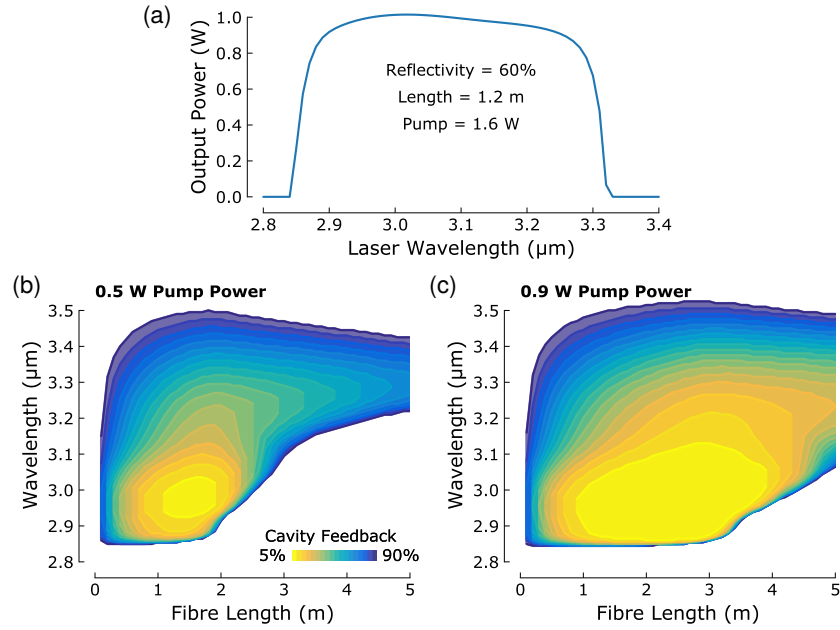


FIGURE 13.10 Simulated CW Dy laser wavelength tunability. (a) Variation of output power as the signal wavelength is varied. Simulated laser tuning range as a function of fibre length and cavity reflectivity for (b) 0.5 W and (c) 0.9 W pump power. Shaded regions indicate where lasing is achieved for the given operating parameters. Adapted from Ref. [4].

gain) at the long wavelength edge.

For mid-IR lasers for sensing applications, wide tunability is a key criterion, and indeed, such modelling was recently performed to optimize the tunability of a Dy:ZBLAN swept-wavelength laser for ammonia sensing [4]. To explore the dependence of tuning range on fibre length, cavity feedback and pump power, an ensemble of simulations were performed. The results are plotted as heatmaps in Fig. 13.10(b)–(c) using coloured regions to indicate the minimum cavity feedback required to achieve lasing at a given wavelength and fibre length. With a limited choice of components in the laboratory, such heatmaps provide a useful visualisation of performance as a function of multiple parameters, and thus enable more efficient selection of laser parameters to achieve a particular output. Detailed discussion of the underlying physics for the observed behaviour in Fig. 13.10 can be found in Ref. [4].

13.2.8 Transient Solutions: Modelling Dynamic Systems

Transient (i.e. time-dependent) solutions are required to model pulsed operation of a laser such as gain-switching or Q-switching. In these cases, conditions that were applied in the steady-state solutions in Sec. 13.2.6.1 (i.e. $d\mathbf{N}/dt = 0$), are no longer valid and the task is to find the solutions for the atomic populations $\mathbf{N}(z, t)$ and powers $\mathbf{P}(z, t)$ in both space z and time t . This is an initial value problem, where evolution of the system in time is obtained from its initial state and the known dynamics that are described by the rate equations. Any external conditions that are changing with time, such as e.g. pump power modulation in gain-switching or cavity loss modulation in Q-switching, also need to be included into the model.

To solve an initial value problem of the atomic system $d\mathbf{N}(z, t)/dt$, iterative numerical methods are generally applied. They work by approximating the future state $\mathbf{N}(z, t + \Delta t)$ from the current state $\mathbf{N}(z, t)$ in small time increments Δt , according to the differential equation $d\mathbf{N}(z, t)/dt$. Since the equations in the laser rate models include terms that can lead to rapid variation in time, *stiff* methods that are adapted to such properties are usually required to avoid numerical instabilities in the solving algorithm. Additionally, it is worth noting that while the spontaneous emission term (Eqn. 13.9) can often be neglected for CW lasers / steady-state modelling, it can be important to include it for transient modelling, since this spontaneous emission can seed the amplification process that describes the light build-up in the cavity.

The equations describing evolution of optical powers (Eqn. 13.8) do not contain an explicit time dependence; the dependence is in the atomic system to which they are coupled. To efficiently solve these equations, we note that the two dimensions, t and z , are coupled by the group velocity of light in the fibre, v_g . The fibre is thus discretised into longitudinal segments of length Δz corresponding to a time step $\Delta t = \Delta z/v_g$. The changes in the atomic population and power evolution equations can then be integrated in time using a fixed-step 4th-order Runge-Kutta method, where the power values at each position are shifted one distance step along the fibre each time step. Note that in this ‘synchronous’ approach, the time step is proportional to segment length—thus, increasing the number of segments at some fixed fibre length will also result in a shorter time step.

For example, one can set all the initial atomic population into the ground state, i.e. $N_0(t = 0) = N_{\text{doping}}$, and $N_i = 0$ for $i > 0$, and set photonic population $\mathbf{P}(t = 0) = 0$ for all length segments. In the next time step, all the powers (of all spectral channels) out of each position element z are entered into the neighbouring spatial segments on each side: $z + \Delta z$ for P^+ channels and $z - \Delta z$ for P^- channels, respectively. Boundary conditions (Eqns. 13.14 & 13.15) are also applied at the first and last spatial segments. Therefore, by including pump power within the boundary conditions, pump light will spread along the full fibre length in the subsequent time steps, and the laser signal will eventually emerge

from the generated inversion and spontaneous emission. Transient solutions can thus offer additional valuable insight into the laser operation, as presented in case studies of Q-switched Dy and Er fibre lasers in the following sections.

A major downside of using transient solutions, however, can be their computational cost. This is particularly exacerbated with the synchronous approach described above, with short fibres and long relaxations times in mid-IR fibre lasers requiring a large number of time steps that may easily exceed tens of millions before the system will reach the steady-state. Simpler numerical algorithms could be relied upon with the already small time step such as RK4, while stiff solvers may have a considerable number of internal steps as well. Typical execution times might be many minutes or even hours for a single run on a modern computer, compared to only seconds often required to solve for steady-state CW operation.

In order to increase the performance of the numerical solving algorithms it can be beneficial to rewrite atomic population and the optical power matrices of all the individual length segments in larger block matrices, therefore having only a single large matrix for each time step. This will markedly increase the size of such matrix, but reduces the number of individual matrix operations as well, which could considerably speed up the computation of each time step (depending on the implementation of the numerical algorithm).

We note here that there is no inherent requirement to enforce the above mentioned synchronization of the space and time step. An asynchronous approach with time step size that is independent from the segment length may also be considered, potentially enabling faster execution by using a larger time step. However, in this case, care must be taken when choosing step sizes to avoid numerical instability of the solving algorithm.

13.2.9 Case Study: Q-Switched Dy:ZBLAN Fibre Laser

To illustrate the application of dynamic laser modelling, we re-visit the example of single-clad Dy:ZBLAN fibre. Specifically, we discuss how the rate equations can be applied to simulate pulsed mid-IR lasers, which have distinct applications to CW systems, for instance in time-resolved sensing such as LIDAR.

For this case study, active Q-switching is employed for pulse generation, whereby an electrically driven switch is placed into the cavity to modulate the intracavity light. Simulation parameters are similar to Section 13.2.7, except that here we use 1.6 m fibre length and a signal wavelength of $3.10\ \mu\text{m}$, to enable comparisons with recent experiments in Ref. [6]. Fig. 13.11(a) shows the practical cavity design including an acousto-optic tunable filter (AOTF), which couples a portion of the incident light into a 1st order diffracted beam. This beam is reflected by a gold mirror, forming the resonant laser cavity, whereas the portion of light which is undiffracted passes out of the device undeflected, thus forming the output beam. The percentage of light which is diffracted depends on the strength of optoacoustic interaction with acoustic waves in the AOTF,

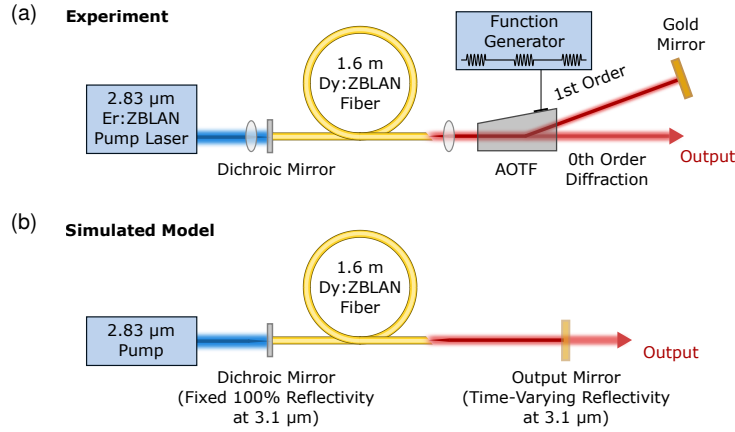


FIGURE 13.11 Dy:ZBLAN Q-switched laser cavity: (a) experimental cavity including AOTF; (b) simplified equivalent cavity which is simulated numerically with a time-varying rear-end reflectivity.

where the acoustic waves are generated by an electrical signal supplied to a built-in transducer. Therefore, by applying a square-wave modulated voltage to the transducer, the AOTF can be operated as a Q-switch, i.e. a fast switch to vary the effective rear mirror reflectivity. Due to a limited phase matching condition, the AOTF also acts as a 5 nm bandpass filter.

To simulate this system, the action of the AOTF and gold mirror are modelled as a rear output mirror with a time-varying reflectivity [Fig. 13.11(b)]. The reflectivity varies between 0 and 28%, where 28% corresponds to the estimated maximum re-injected power when the AOTF is on (accounting for AOTF diffraction efficiency and coupling losses). Due to the finite AOTF rise time, τ_{rise} , there is a 25 μs delay between the electrical signal being applied and the acoustic wave building up, which we model as a linear increase in cavity reflectivity from 0 to 28% over a 25 μs period from the moment an electrical signal is applied.

As in the CW Dy:ZBLAN case study, only one pump and one signal channel are defined in the model (but for both directions). However, we now also include spontaneous emission since this can be important for accurately simulating the initial build-up of light. This is achieved by including the spontaneous emission term (Eqn. 13.9) and choosing a spectral channel width of $\Delta f = 5$ nm, which corresponds to the filter bandwidth of the AOTF (i.e. effective system gain bandwidth). The numerical model is then solved using the synchronised space-time approach described in Section 13.2.8; we note that execution times are typically on the order of minutes for an implementation using Python running on a personal computer.

We first consider the radiation build-up dynamics of the Q-switched laser. A 2 kHz modulation function is applied, comprising of voltage signals lasting 16 μs per cycle (i.e. 3.2% duty cycle; we refer to this as ‘modulator “on” time’

τ_{ON}) and from $t = 0$, the fibre is continuously pumped through the front facet by a CW 2.83 μm laser with 0.6 W power. The impact of the AOTF rise-time and modulation parameters are discussed later, enabling us to focus initially on the temporal evolution of laser properties that lead to stable pulsation, as shown in Fig. 13.12.

The simulation shows that at $t = 0$, the ground state is fully occupied ($N_0 = N_{\text{doping}}$, or in terms of normalised population densities, $n_0 = 1$). As CW pump light starts to be injected at this time, n_0 begins to fall as Dy ions are excited into the upper manifold (i.e. increased n_1 occupancy). The populations plateau after $\sim 500 \mu\text{s}$ due to pump saturation. During this time, the cavity is not lasing and the output power is effectively negligible. Even while a resonant cavity is formed during the first few modulation cycles (i.e. when the reflectivity goes high), the laser output remains low as intracavity signal power has yet to build up sufficiently to initiate lasing in this time window.

After $\sim 1 \text{ ms}$, output pulses are generated during subsequent modulator ‘on’ cycles. The first few pulses to be emitted, however, are not stable: the power of each pulse fluctuates. After $\sim 2 \text{ ms}$, the laser settles into a steady-state periodic Q-switched output, with identical pulses generated each modulation cycle. The temporal population evolution shows that each output pulse is accompanied by a small drop in upper state population n_1 (due to depopulation by stimulated emission), which is gradually recovered by absorption of the CW pump input over the remaining cycle time while the modulator is off. Practically, the pulse properties of Q-switched lasers in the steady state are of greatest interest. Therefore, when discussing Q-switched laser performance, we only consider the pulses properties after 3 ms simulation time, to ignore the noisy transient pulses in the initial build-up phase. These pulse properties are now examined in more detail.

Fig 13.13(a) shows the experimentally measured Q-switched output with $\tau_{\text{ON}} = 16 \mu\text{s}$ AOTF on-time at 0.6 W pump power and 2 kHz modulation frequency (after Ref. [6]). Note that the measured time-dependent reflectivity is also shown, which is reasonably approximated in simulations as a linear time-delayed reflectivity change. Modelling outcomes with these input conditions also showed stable single pulse operation [Fig 13.13(b)], producing symmetrical pulses with 330 ns duration, 14.1 μJ energy and 36 W peak power. Such properties are in reasonable agreement with the experimentally measured values of 275 ns, 11.5 μJ , 39 W.

With a longer AOTF on-time (i.e. longer duty cycle) of $\tau_{\text{ON}} = 50 \mu\text{s}$, the simulation also captures the experimental observation of satellite pulses being produced after the main pulse within each modulation cycle [Fig. 13.11(c)–(d)]. This is an unwanted phenomena which limits the pulse peak power and could cause timing errors in applications such as time-resolved sensing.

Having confirmed that the simulation is well matched to experimental results, the model can then be used identify routes to improved Q-switched laser performance: specifically, identifying how to achieve greater pulse peak powers. It is known that there are numerous possible causes for multipulsing in pulsed

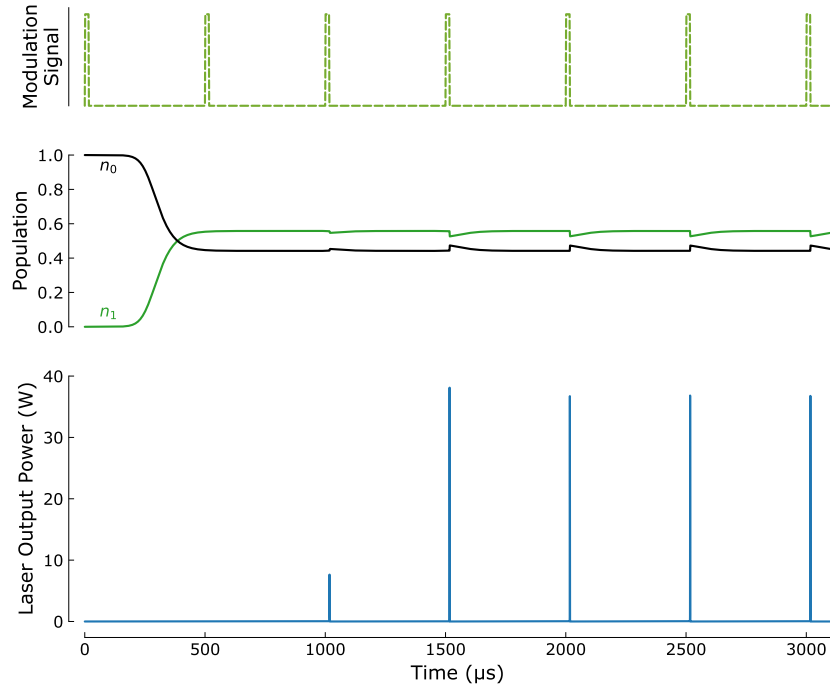


FIGURE 13.12 Dy:ZBLAN 2 kHz Q-switched laser simulation start-up dynamics. The modulator on-time is 16 μs per cycle, shown by the short bursts of increased rear-mirror reflectivity. The pump is applied at $t = 0$, causing the inversion to build-up (normalised upper state population n_1 increases). Note that no pulses are generated for the first few modulation cycles, but after ~ 2 ms, the laser settles into a steady Q-switched operation, generating a stable pulse train.

lasers, and a solution was sought to avoid this. Specifically, the model permitted testing of the hypothesis that the primary cause was the slow switching speed of the modulator. This could be explained physically by the fact that after the electrical MHz drive signal is applied to the AOTF, the cavity loss reduces over a period of $\tau_{\text{rise}} = 25 \mu\text{s}$ as acoustic waves slowly build-up and diffract light towards the cavity mirror. A pulse will start building-up in the cavity, however, as soon as the loss falls below the amount of stored gain, which can be before the AOTF has finished switching. In this case, the pulse build-up can be faster than the rate of switching, forming a complete pulse before the cavity loss minima is reached. Residual inversion remains in the doped fibre, therefore, and as the loss continues to gradually fall, the emission process repeats to extract this energy: thus forming multiple low-energy pulses per Q-switching cycle [7].

By repeating simulations with the modulator rise time reduced to $\tau_{\text{rise}} = 1 \mu\text{s}$, substantial improvement was observed [Fig. 13.11(e)]. The model predicted the generation of a single pulse per modulation cycle with 90 ns duration, 49 μJ pulse

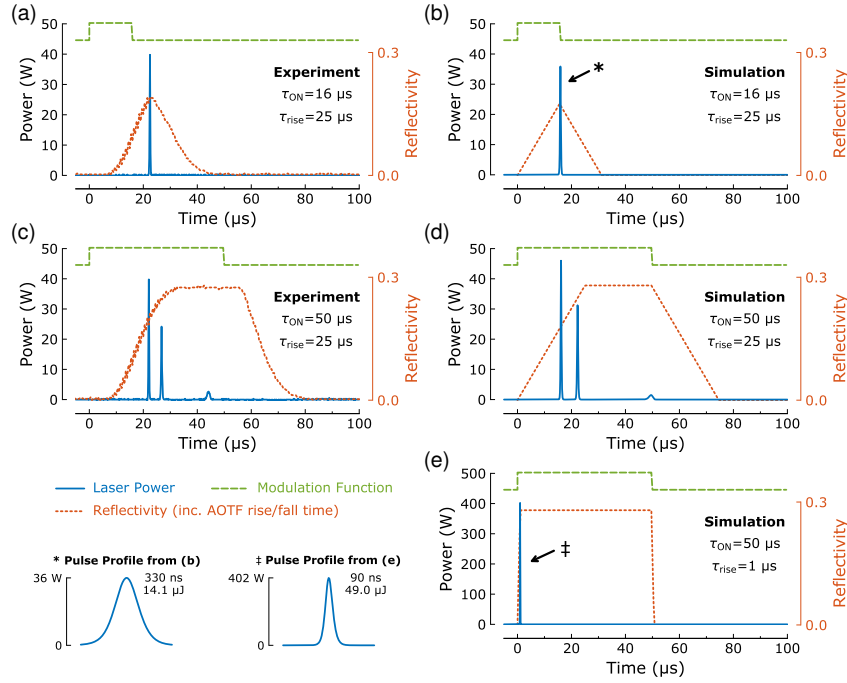


FIGURE 13.13 Steady-state dynamics actively Q-switched 3.1 μm Dy laser with 0.6 W pump power: (a) experimental and (b) simulated single-pulse operation with optimum $\tau_{\text{ON}} = 16 \mu\text{s}$ AOTF on-time; (c) experimental and (d) simulated multi-pulse operation with $\tau_{\text{ON}} = 50 \mu\text{s}$; (e) simulated single-pulse operation with 50 μs on-time but a faster modulator rise time of $\tau_{\text{rise}} = 1 \mu\text{s}$. Adapted from: Ref. [6].

energy and 402 W peak power—over an order of magnitude improvement. This shows that with faster switching, a single pulse ‘sees’ larger gain available during its build-up time and thus, can extract significantly more energy. Multi-pulsing is therefore avoided.

This example demonstrates the utility of numerical modelling for offering additional insight beyond experimental measurements, in addition to permitting exploration of arbitrary parameter spaces to identify improved laser designs. For this example, simulation results paved the way to a higher energy Q-switched laser design by suggesting the AOTF to be replaced by a faster acousto-optic modulator (which are already commercially available, although this has yet to be implemented). Without such a numerical model, it may have taken considerably more experimental effort, time and financial resources to reach such a conclusion.

13.2.10 The Er Fibre Laser: Modelling Complex Systems

The energy level structure of Er is significantly more complex than Dy and many levels must be included in models for mid-IR Er lasers. Weak non-radiative processes in low-phonon-energy glasses such as ZBLAN result in long effective lifetimes, allowing significant atomic population to be established in excited levels high above the ground state. Energy transfer (ET) processes such as energy-transfer upconversion (ETU) and cross-relaxation (CR) are also often present in Er lasers, which couple to those high lying levels, making it necessary to include them in the rate equation model. The energy levels and currently known transitions in Er:ZBLAN fibre that are relevant for both laser operations at 2.8 μm and 3.5 μm are illustrated in Fig. 13.14.

The fibre lasers in the two case studies that follow are quite different from each other in term of laser design and operation schemes, but in their models they are distinguished only by a minor number of parameters. In fact the Er laser in the case study at 3.5 μm based on a recently developed scheme with dual wavelength pumping also includes a nascent laser operation at 2.8 μm . Thus having 2 pumps, 2 signals and 7 levels in Er makes it a worthy showcase of a complex system that is well suited for the matrix modelling formulation as introduced in Sec. 13.2.3. The model of a heavily doped Er:ZBLAN fibre laser at 2.8 μm featured in the last case study is of comparable numerical complexity, and we use it to demonstrate how such models can help with validation of known, or determination of unknown, parameters and their values.

Values for all the parameters used in the model for both Er fibre laser cases are given in Tables 13.2 and 13.3. Table 13.2 includes the parameters constituting the linear part of the rate equation system (Eqns. 13.11 and 13.12), including all radiative and non-radiative transfers except the energy transfer processes, as well as fibre laser design properties for both cases. Values of the parameters that were not given or are not relevant for the case are omitted, while the values that are relevant, but were unknown when these model studies were conducted, are given in brackets.

The parameters of the energy transfer (ET) processes w_{ijkl} that describe the transition from initial levels i and j to levels k and l form the nonlinear part of the rate equation system (Eqn. 13.13). The values of the three ET parameters, w_{1103} , w_{2206} , and w_{5031} were measured in bulk at different Er concentrations [19]. A model-based study has shown these ET processes to be beneficial for laser operation, enabling an efficient *energy recycling* regime with slope efficiencies reaching above 50% in heavy doped fibres [20].

However, significantly weaker ET parameters were later proposed based on a comparison of a model with a fibre laser experiment [1]. The former became known as the *strongly interacting* (SI) and the latter as the *weakly interacting* (WI) models, i.e. higher or lower values of the same ET parameters that are given in Table 13.3 for two doping concentrations corresponding to fibres used in the two case studies. We should note that the ET parameters are not expected

TABLE 13.2 Linear model parameters of the Er:ZBLAN fibre lasers

Parameter	Symbol	Case Study at 3.5 μm	Case Study at 2.8 μm
Relaxations		from Ref. [5]	same as in Case at 3.5 μm
Effective lifetimes	τ_1, τ_2, τ_3	9.9 ms, 7.9 ms, 8 μs	
	τ_4, τ_5, τ_6	177 μs , 530 μs , 5 μs	Same as left-hand column
Branching ratios	$\beta_{21}, \beta_{20}, \beta_{32}$	0.182, 0.818, 0.999	
	$\beta_{30}, \beta_{43}, \beta_{42}$	0.001, 0.808, 0.008	
	$\beta_{41}, \beta_{40}, \beta_{54}$	0.009, 0.175, 0.285	
	$\beta_{53}, \beta_{52}, \beta_{51}$	0.029, 0.014, 0.193	
	$\beta_{50}, \beta_{65}, \beta_{60}$	0.479, 0.990, 0.010	
Cross-sections		from Ref. [5]	from Ref. [1]
Pump 1 wavelength	λ_{p1}	985 nm	976 nm
Pump 1 absorption	$\sigma_{02}(\lambda_{p1})$	$9.3 \times 10^{-26} \text{ m}^{-3}$	$21.0 \times 10^{-26} \text{ m}^{-3}$
ESA 1a	$\sigma_{26}(\lambda_{p1})$	$2.0 \times 10^{-26} \text{ m}^{-3}$	$11.0 \times 10^{-26} \text{ m}^{-3}$
ESA 1b	$\sigma_{36}(\lambda_{p1})$	$25.5 \times 10^{-26} \text{ m}^{-3}$	
Pump 1 emission	$\sigma_{20}(\lambda_{p1})$	$11.5 \times 10^{-25} \text{ m}^{-3}$	$16.1 \times 10^{-26} \text{ m}^{-3}$
	$\sigma_{62}(\lambda_{p1})$	$6.75 \times 10^{-26} \text{ m}^{-3}$	$21.1 \times 10^{-26} \text{ m}^{-3}$
	$\sigma_{63}(\lambda_{p1})$	$47.8 \times 10^{-26} \text{ m}^{-3}$	$17.4 \times 10^{-26} \text{ m}^{-3}$
Pump 2 wavelength	λ_{p2}	1973 nm	
Pump 2 absorption	$\sigma_{24}(\lambda_{p2})$	$30.0 \times 10^{-26} \text{ m}^{-3}$	$30.0 \times 10^{-26} \text{ m}^{-3}$
Pump 2 emission	$\sigma_{42}(\lambda_{p2})$	$36.1 \times 10^{-26} \text{ m}^{-3}$	$36.1 \times 10^{-26} \text{ m}^{-3}$
ESA2 from [3], SI	$\sigma_{46}(\lambda_{p2})$	$(0.7 \times 10^{-26} \text{ m}^{-3})$	
Signal 1 wavelength	λ_{s1}	2800 nm	2800 nm
Signal 1 absorption	$\sigma_{12}(\lambda_{s1})$	$9.5 \times 10^{-26} \text{ m}^{-3}$	$4.7 \times 10^{-26} \text{ m}^{-3}$
Signal 1 emission	$\sigma_{21}(\lambda_{s1})$	$17.1 \times 10^{-26} \text{ m}^{-3}$	$8.1 \times 10^{-26} \text{ m}^{-3}$
Signal 2 wavelength	λ_{s2}	3470 nm	
Signal 2 absorption	$\sigma_{43}(\lambda_{s2})$	$6.9 \times 10^{-26} \text{ m}^{-3}$	
Signal 2 emission	$\sigma_{43}(\lambda_{s2})$	$5.2 \times 10^{-26} \text{ m}^{-3}$	
Fibre laser parameters		from Ref. [5]	from Ref. [1]
Doping concentration	N_{doping}	$2.7 \times 10^{26} \text{ m}^{-3}$	$9.6 \times 10^{26} \text{ m}^{-3}$
Fibre length	L	0.18 m	4.0 m
Core area	A_{core}	$0.87 \times 10^{-10} \text{ m}^{-2}$	$3.0 \times 10^{-10} \text{ m}^{-2}$
Overlap factors	$\Gamma(\lambda_{p1})$	0.96	0.009
	$\Gamma(\lambda_{p2})$	0.83	
	$\Gamma(\lambda_{s1})$	0.62	1.0
	$\Gamma(\lambda_{s2})$	0.41	
Background losses	$l(\lambda_{p1})$		$3.0 \times 10^{-3} \text{ m}^{-1}$
	$l(\lambda_{s1})$		$23.0 \times 10^{-3} \text{ m}^{-1}$
	$l(\lambda_{s2})$	$60.0 \times 10^{-3} \text{ m}^{-1}$	
Mirror reflectivities	$R^-(\lambda_{p1}), R^+(\lambda_{p1})$		0.04, 0.04
	$R^-(\lambda_{s1}), R^+(\lambda_{s1})$		0.04, 0.96
	$R^-(\lambda_{s2}), R^+(\lambda_{s1})$	0.87, 0.99	

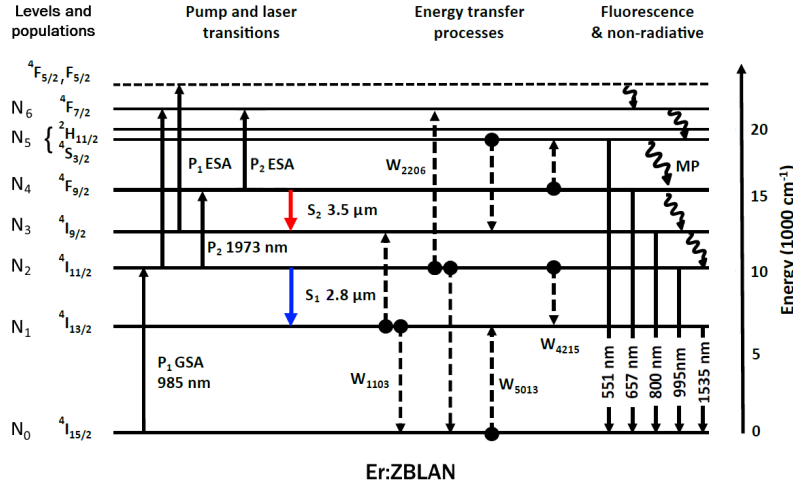


FIGURE 13.14 Energy levels and transitions in Er:ZBLAN fibre laser operation at 2.8 μm or dual-wavelength pumped at 3.5 μm . Level populations are denoted as used in the models for both of those lasers and their spectroscopy designations are given on the left. The transfer processes include pump and laser transitions from the ground state absorption (GSA), excited state absorptions (ESA) for pump at both wavelengths P_1 and P_2 , and laser signals S_1 and S_2 , and energy transfer processes among two ions. Many radiative (fluorescence) and non-radiative multi-phonon (MP) relaxation processes are omitted from the diagram, but are included in the model through their branching ratios as can be read from Table 13.2. Adapted from [5].

to differ between bulk and the fibre made out of the same material, therefore the exact causes for this discrepancy are not yet fully understood.

Recently a fourth ET parameter w_{4251} was discovered [21] and its value was found to be only slightly dependent on the Er doping concentration. However, because the other three ET parameters were relied upon in its determination process, two distinct values were reported to go with with SI and WI parameters [21]. A new excited state absorption process was also found after that study, that causes quenching of the laser operation at 3.5 μm [3] and this is also included in Table 13.2 for completeness, although it was not used in this case study. It may therefore have some implications in determining the values of other processes, in particular w_{4251} .

13.2.11 Case Study: Dual-wavelength pumped Er Fibre Laser at 3.5 μm

The dual-wavelength (DWL) pumping technique [22] takes advantage of the long lifetime of level $^4I_{11/2}$ in Er, which is level N_2 in our model (see Fig. 13.14). The first pump at wavelength around 980 nm (P_1) is to excite ions from the ground

TABLE 13.3 Energy transfer parameters of the Er:ZBLAN fibre lasers

Parameter	Symbol	Case study at 3.5 μm	Case study at 2.8 μm
Doping concentration	Er	1.7% mol	6% mol
Doping number density	N_{doping}	$2.7 \times 10^{26} \text{ m}^{-3}$	$9.6 \times 10^{26} \text{ m}^{-3}$
Strongly interacting (SI)		from [21]	
ETU1 (SI values)	w_{1103}	$1.4 \times 10^{-24} \text{ m}^3 \text{ s}^{-1}$	$3.6 \times 10^{-23} \text{ m}^3 \text{ s}^{-1}$
ETU2 (SI values)	w_{2206}	$0.3 \times 10^{-24} \text{ m}^3 \text{ s}^{-1}$	$1.2 \times 10^{-23} \text{ m}^3 \text{ s}^{-1}$
CR1 (SI values)	w_{5031}	$0.8 \times 10^{-24} \text{ m}^3 \text{ s}^{-1}$	$2.7 \times 10^{-23} \text{ m}^3 \text{ s}^{-1}$
CR2 (SI values)	w_{4251}	$2.5 \times 10^{-23} \text{ m}^3 \text{ s}^{-1}$	$(3.6 \times 10^{-23} \text{ m}^3 \text{ s}^{-1})$
Weakly interacting (WI)		from [21]	
ETU1 (WI values)	w_{1103}	$0.4 \times 10^{-24} \text{ m}^3 \text{ s}^{-1}$	$1.0 \times 10^{-24} \text{ m}^3 \text{ s}^{-1}$
ETU2 (WI values)	w_{2206}	$0.1 \times 10^{-24} \text{ m}^3 \text{ s}^{-1}$	$0.3 \times 10^{-24} \text{ m}^3 \text{ s}^{-1}$
CR1 (WI values)	w_{5031}	$0.2 \times 10^{-24} \text{ m}^3 \text{ s}^{-1}$	$0.5 \times 10^{-24} \text{ m}^3 \text{ s}^{-1}$
CR2 (WI values)	w_{4251}	$1.7 \times 10^{-23} \text{ m}^3 \text{ s}^{-1}$	$(1.4 \times 10^{-23} \text{ m}^3 \text{ s}^{-1})$

level N_0 into N_2 , which acts as an elevated ‘virtual’ ground state. The second pump at wavelength around 1975 nm (P_2) is then further exciting the ions into N_4 . Lasing at 3.5 μm takes place between levels N_4 and N_3 , while N_3 is subject to rapid decay back into N_2 . Such operation is significantly more efficient than pumping from the real ground level, since less power is wasted by decay from N_2 to the ground state N_0 and only a small amount of power P_1 is needed to maintain an inversion. At low P_2 powers, lasing at 2.8 μm on the $^4I_{11/2} \rightarrow ^4I_{13/2}$ transition between levels N_2 and N_1 appears as well.

A numerical model of the DWL pumped laser at 3.5 μm was developed at University of Adelaide [5] and implemented in the MATLAB programming environment using the RK4 method with the synchronous transient approach. At each time step the new transition rates based on the previous state and new states, based on the new rates, were calculated for the whole system, i.e. all populations and powers in all segments, concurrently. These *rate* and *state* matrices were written in two larger 2D block matrices to speed up the calculations as discussed in Sec. 13.2.8. Results were saved in into one 3D state-time matrix at reduced temporal resolution to save memory.

Multiple simulation instances were run concurrently on a ‘Phoenix’ high performance computer provided by the University of Adelaide. A multi simulation session took 5 hours using 10 longitudinal segments and solving for 20 ms in the model, which is comparable to simulations run on a desktop PC with concurrency up to the number of its cores. The modelling results were then tested on three previously published experiments and good agreement was found with all of them using the WI set of ET parameters from the Table 13.3. Another successful study was reported later for the Q-switching operation using the same model [23].

Here we present some basic results from modelling one of those experiments, using a single-clad Er:ZBLAN fibre with 1.7% mol Er-doped core, 10.5 μm

diameter. All the parameters required to describe the particular fibre laser design are listed at the bottom of Table 13.2. Eight optical channels (elements of the power matrix) were used in this model altogether, two for each pump P_1^+ and P_2^+ , and two for each laser transition S_1^+ and S_2^+ at 2.8 μm and 3.5 μm , respectively. Pump powers in ‘+’ direction are launched into the front end of the fibre ($z = 0$) and the output coupler is located at the rear end of the fibre ($z = L$). Therefore, the output powers of the transmitted signals are also the ‘+’ direction. Spontaneous emission was included in the model to initiate lasing on both transitions, therefore simulating realistic starting of the laser and competition between both transitions, as this aspect is important in design optimization of such lasers.

First, the development of the steady-state state condition is studied after turning on constant pumping with both pumps, P_1 and P_2 , from a single end at input powers 194 mW and 2 W, respectively. This is set in the model by initializing all populations N and laser signal power S_1 and S_2 to zero, while setting the boundary conditions of $P_1^+(z = 0) = 194 \text{ mW}$ and $P_2^+(z = 0) = 2 \text{ W}$. The temporal evolution of Er energy level populations in segment no. 5 in the middle of the fibre are shown in Fig. 13.15, as that segment is most representative for all 10 segments. The longitudinal dependence of all parameters (not shown) is similar to the Dy cases, stemming from the characteristic quasi-exponential pump absorption in single end fibre pumping. The intracavity power of the laser signal S_2^+ in the same segment propagating in the ‘+’ direction at 3.5 μm is also shown in the same figure. Note that significant laser power starts at $t = 1 \text{ ms}$, after the start of the pumping process at $t = 0 \text{ ms}$, thus showing the time it takes to build up enough population inversion in levels N_4 and N_3 to overcome the losses (threshold condition). The laser power rises much faster than the populations after that time.

A significant population builds in level N_1 due to its long effective lifetime $\tau_1 = 9.9 \text{ ms}$ and weakly interacting ET processes, resulting in about 20 ms for the system to reach the steady-state in these conditions. Note that a snapshot of the populations and powers in this last instant (or any time after that) will be equal to the solutions that could be obtained via methods adapted directly for the steady-state as presented in Sec. 13.2.6. Such approach would most likely be faster, i.e. requiring significantly less computational time, but all the temporal dynamics that follows in the rest of the Er case studies would not be obtained with such an approach.

With all the transient information available, however, it is instructive to have a closer look at the starting of the laser even for CW operation, i.e. having the same constant (CW) pump power as before. In Fig. 13.16(a) the initial transient of the intracavity laser powers for both transitions S_1^+ at 2.8 μm and S_2^+ at 3.5 μm are displayed in the same mid segment, where CW pump power starts abruptly at $t = 0 \text{ ms}$. Relaxation oscillations appear at both transitions, and are more pronounced with S_1 signal due to higher cross-sections for that transition compared to S_2 signal. It is also worth noting that a small amount of

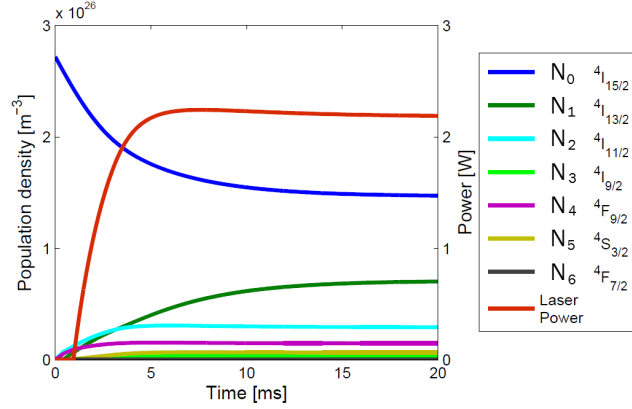


FIGURE 13.15 Temporal evolution of Er energy level populations and intracavity laser power of S_2^+ at $3.5\mu\text{m}$ from the model in the segment no. 5 in the middle of the fibre after turning on both pumps, P_1 and P_2 , at time $t = 0$ ms. Adapted from [5].

power remains in the S_1 signal channel (20 mW intracavity power in this case) even after S_2 builds up and acts to suppress S_1 , the amount depending on the P_2 power.

An interesting phenomenon that was also observed experimentally in Ref. [5] appears in pulsed operation of this laser when P_2 pump is pulsed at low powers. Results from the model of such behaviour are shown in Fig. 13.16(b), where the P_2 pump power was set to operate in 300 μs long square-shaped pulses with a frequency of 1 kHz and 200 mW peak power. Signal S_1^+ at $2.8\mu\text{m}$ is starting first again, featuring a single spike from relaxation oscillations and running longer than the pump in each single pulse. At 4 ms, a signal S_2^+ at $3.5\mu\text{m}$ starts to appear that is only about 100 μs long, much shorter than the pump, and it always appears alternatively with S_1 . Transient modelling is thus very helpful in studying the effects of laser design and operational parameters on laser pulse formation, including optimisation of output pulse durations/peak powers.

After having shown some details that transient models of such system can capture, we now approach a more practical problem. That is, for example, to study the input-output power characteristics of the fibre laser as a function of P_2 pump power while holding P_1 constant at 194 mW. The results shown in Fig. 13.17(a) are in reasonable agreement with the experiments performed in [22] for both CW and pulsed operation. The threshold power obtained from the model of slightly above 100 mW matches experiments well. The slope efficiencies at lower P_2 powers and the appearance of roll-over at higher P_2 powers are also in agreement with the experiment. However, the model predicts less significant saturation with increasing P_2 than observed experimentally, with

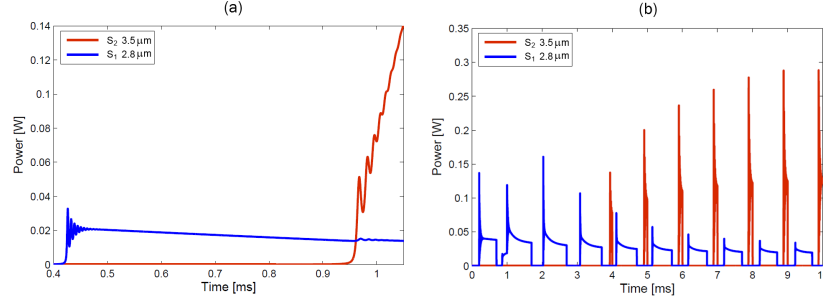


FIGURE 13.16 (a) Simulated results for the intracavity powers of both laser signals S_1^+ at 2.8 μm and S_2^+ at 3.5 μm with CW pumping after starting both pumps, P_1 and P_2 at $t = 0$ ms in the model. (b) Simulated results for both intracavity powers S_1^+ at 2.8 μm and S_2^+ at 3.5 μm with constant P_1 and pulsed P_2 with 300 μs long pulses at frequency 1 kHz, starting at $t = 0$ ms. Adapted from [5].

larger discrepancy in the pulsed regime. The authors note in Ref. [5] that this could be explained due to the thermally induced misalignment of the fibre tip to the butt-coupled mirror in their experiment, effectively reducing the signal reflectivity at the boundary.

Transmitted pump powers P_1^+ and P_2^+ that emerge from the fibre end opposite to the pump input can be measured and used as additional validation of the modelling results. As shown in Fig. 13.17 (b) there is a good agreement between modelled and experimental data for both pumps. Nearly all of the power in P_1^+ is absorbed in the fibre, while the absorption of P_2^+ is decreasing—note the slight change in slope around $P_2 \sim 1$ W, which corresponds to the start of roll-over in the signal power S_2 .

The absorption of P_2 depends on the cross-sections $\sigma_{24}(\lambda_{p1})$ and $\sigma_{42}(\lambda_{p1})$ and populations N_2 and N_4 . In Fig. 13.17(c), populations of all levels in the model are plotted, averaged over the entire fibre length. There is a steep decrease in N_2 and increase in N_4 below the laser threshold powers of P_2 , but there is imperfect clamping above the threshold, which causes saturation of the laser power S_2 .

In order to learn more about the underlying level population dynamics, one can calculate the actual rates of all the transfer processes from the model results. Most important are the one that are directly involved in the dynamics of the laser levels, namely N_2 ("virtual ground state"), N_3 (lower laser level) and N_4 (upper laser level). Discussion of these intricacies is outside of the scope of this Chapter, however, and the reader is kindly referred to Refs. [5, 23] for further information.

Instead we show in Fig. 13.17(d) the results from the model with variation of the two most influential parameters: the lifetime of level 3, τ_3 , and the energy transfer process w_{4251} . The results clearly show that a dominant limitation on

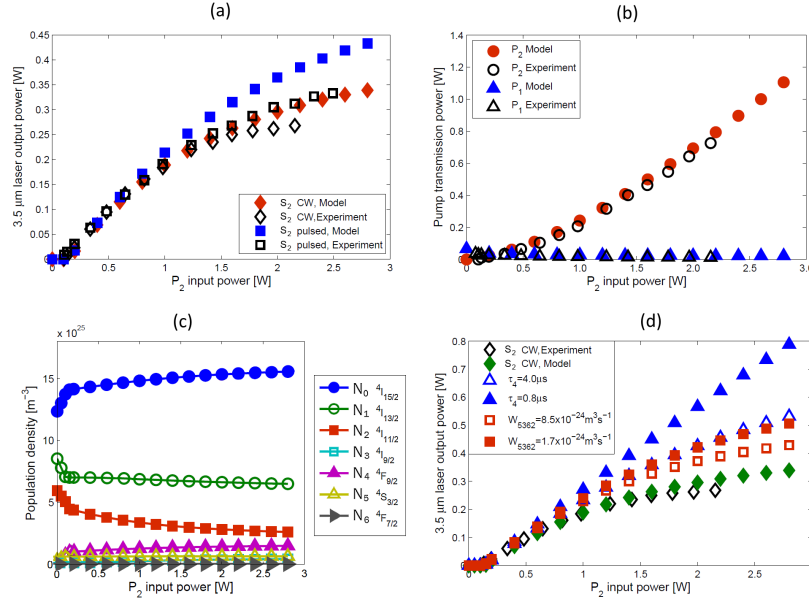


FIGURE 13.17 (a) Laser output power from modelling results and experimental measurements in CW and pulsed pump regimes. (b) Transmitted (unabsorbed) pump powers P_1 at 985 nm and P_2 at 1973 nm from modelling results and experimental measurements in CW pump regimes. (c) Populations of all levels averaged over the entire fibre length. (d) Comparison of the measured laser power and model results with reducing parameters τ_3 and w_{4251} from their nominal values of 8 μs and $1.7 \times 10^{-23} \text{ m}^3 \text{ s}^{-1}$, respectively. Adapted from [5].

laser performance is the accumulation in N_3 , since that is alleviated by reducing the lifetime τ_3 by an arbitrary factor of 8 (and thus increasing the transfer rate by the same factor), while w_{4251} is shown to have a significant effect as well.

13.2.12 Case Study: Heavily doped Er:ZBLAN Fibre Laser at 2.8 μm

Laser operation at 2.8 μm alone is simpler than in the previous case, with pump transition P_1 from the ground state N_0 into N_2 , and laser transition between the populations $N_2 \rightarrow N_1$ as illustrated in Fig. 13.14. Therefore this would be a simple four-level laser in the absence of the transitions from the excited states, and such conditions indeed appear at very low doping concentrations. However, because of the long lifetime τ_1 , which is even longer than τ_2 , this creates a population bottleneck in N_1 that causes the laser operations to be *self-terminating*. At high doping concentrations, however, the energy transfer (ET) processes between neighbouring ions become strong enough to alleviate this bottleneck to largely drive the depopulation process, thus enabling efficient CW

laser operation. Knowing the values of these parameters is therefore crucial in modelling and understanding the laser operation, both at 2.8 μm and also 3.5 μm as discussed in the previous case.

We devote this last case study for brief a look into role of the ET parameters in the operation at 2.8 μm , with w_{1103} , w_{2206} and w_{5031} included, while w_{4251} was not included as it was not yet known at the time. Nonetheless all their values are included in Table 13.3 for completeness. We should stress at this point that it is not the intent of this section to present and explain all of the many other effects that are also involved, as that is covered in other chapters of this book and in the references provided here. Our intent is only to offer a glimpse of how the modelling, and in particular the transient solutions, can offer useful insight into this problem.

The fibre laser setup used in this case study comprised fibre with 30 μm core diameter, doped with 6% mol Er, and D-shaped cladding with effective diameter of 350 μm . The cavity is composed of a 4 m long doped fibre, with feedback provided by Fresnel reflection at the front end ($z = 0$) and a broadband HR mirror at the rear end ($z = L$), thus forming a free-running CW fibre laser. The diode pump P_1 at 976 nm wavelength is coupled into the cladding from the front side propagating in the '+' direction, while the signal S_1 is confined to the core and S_1^- is coupled out at the front end.

Note that this is essentially the same Er rate equation model as described in the previous case with dual-wavelength pumping and operation on 3.5 μm transition, except for the differences in the fibre laser design parameters as described above and collated in Table 13.2, as well as not using second pump P_2 and second signal S_2 . Transient solutions were obtained with similar space-time synchronous approach as in the previous case.

The results from the model are shown in Fig. 13.18(a) and (b) where CW input pump power P_1^+ is applied from 0 to 15 ms using both SI and WI parameters, respectively. Shorter pump pulse duration (15 ms) than the total simulated time (20 ms) was chosen, in order to study both transients, when the laser (pump) is switched on and also when it is switched off.

In both of these cases the laser output signal S_1^- starts almost instantly and with strong relaxation oscillations. It reaches steady state in less than 15 ms. The rise time and the final (CW) power of the signal is markedly different in both regimes.

Fluorescence signals can offer additional insight into the dynamics of atomic populations since fluorescence emitted at distinct wavelengths is proportional to population in individual corresponding levels. Obtaining accurate absolute relations can be very difficult in practice, but the relative (normalized) dynamics is straightforward. In Fig. 13.18(a) and (b) the dynamics of the population $N_5(t)$ normalized to $N_5(t = 15 \mu\text{s})$ are shown, which correspond to fluorescence at 551 nm. This fluorescent line is dominant in Er lasers, and N_5 is strongly coupled to both laser levels N_1 and in particular N_2 (see Er level diagram in Fig. 13.14). Fluorescent lines at 1535 nm and 995 nm that correspond directly to N_1 and N_2

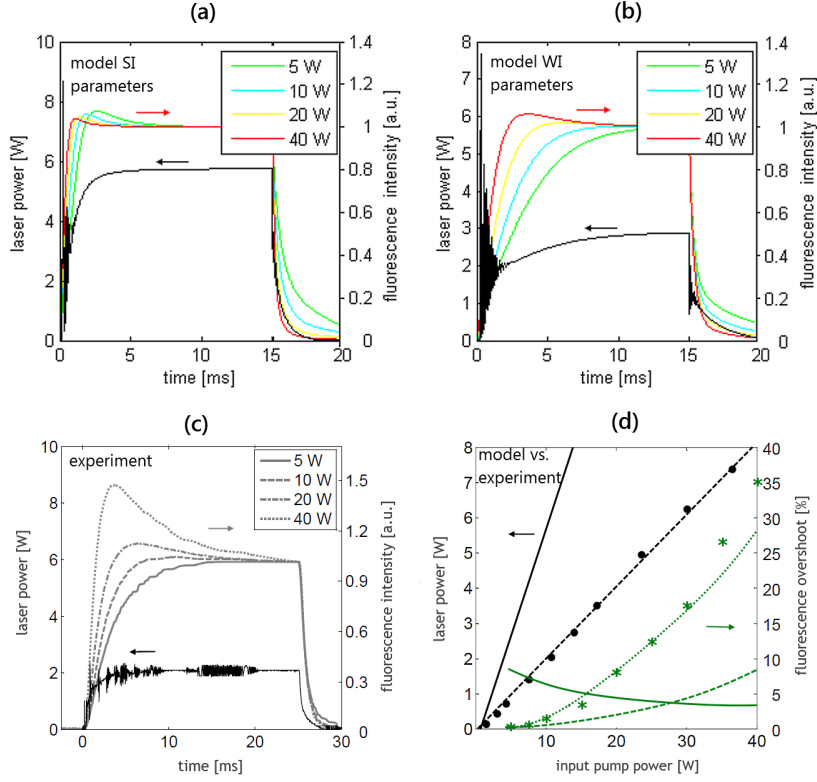


FIGURE 13.18 (a) and (b) Transient solutions of the model for laser output signal power S_1^- at $2.8 \mu\text{m}$ (solid black lines) at 10 W input pump power, and normalized N_5 population that is proportional to fluorescence signals is shown for 5–40 W input pump power for both SI (a) and WI (b) values of the ET parameters. (c) Experimental measurement of the same conditions, except for 25 ms of pump on time. (d) Measured laser signal power (black dots) and fluorescence overshoot (green dots), and results from the model with SI (full lines) and WI (dashed lines) parameters. The dotted line is fluorescence overshoot multiplied by 3 obtained with the same WI parameters.

might be considered even better choices, but their time dependent signals turned out difficult to be measured in our experiments.

Experimentally measured transient laser output powers and fluorescent signals are shown in Fig. 13.18(c), where different time scales are to be taken into account. Model results with WI parameters display much better, though far from perfect, agreement with experimental results. Slow fluorescent rise time at low input pump powers, and the trend of increasing overshoot of its steady-state intensity with increasing pump powers only appear with the WI parameters. Such trend is indeed observed experimentally, even more pronounced than in

our model results. The laser threshold, its slope efficiency, rise times of laser and fluorescence signals, the trend of its overshoot are all better matched with the WI parameters as can be seen in Fig. 13.18(d) and Table 13.4.

TABLE 13.4 Modelling results and experimental measurements in Er:ZBLAN fibre laser

Observable parameter	Model SI	Model WI	Measurement
Slope efficiency	49%	22%	21%
Laser threshold	1.2 W	0.4 W	0.5 W
Rise time of the laser signal power	2.2 ms	5.2 ms	3.9 ms
Rise time of the fluorescence signal	1.2 ms	4.4 ms	3.7 ms
Overshoot in the fluorescence signal	4.4%	9.3%	26%
Trend of the overshoot with power	decreasing	increasing	increasing

The WI parameters were in fact set to maximise the overall match between the model results and experimental measurements. Values of many other parameters were also adjusted in the model as part of their validation, in order to evaluate the sensitivity of the model within the range of their uncertainties (a similar approach was carried out in the previous case as well). The three ET parameters w_{1103} , w_{2206} and w_{5031} were found to be the most influential to the efficiency of operation and power scaling of the fibre laser, with ESA $\sigma_{26}(\lambda_{p1})$ having a significant role as well due to the growing populations in both laser levels N_1 and N_2 . Similar behaviour with notable large and increasing green fluorescence overshoot was observed experimentally using other fibres, with two of those coming from a different manufacturer than the fibre used in the fibre laser setup. Furthermore, good agreement with other published experiments to date was found in a subsequent model study using the WI parameters in Ref. [24], which also included the effects of pump and laser wavelengths, and temperature in the fibre core.

We should nonetheless stress that such heuristic approach to finding (or validating) parameters based on any single experiment or otherwise limited dataset may of course result in biased or limited scope of validity of the obtained (calibrated) results. However, when carefully approached and considering a large set of experimental data, this is without doubt a powerful extension of the direct measurement method.

13.3 THERMAL MODELLING

Absorbed pump power that is not converted into the optical signal or emitted out of the fibre as fluorescence, ends up dissipated as heat in the doped core of the fibre. This results in increased temperature of the fibre core, that can in turn have significant effects on laser operation. Many of the processes in laser ions that are included in the rate equation model from previous sections are temperature dependent, in particular the effective cross-sections (although typical rate equation modelling uses input spectroscopic parameters measured

only at room temperature—limiting validity at high operating temperatures). Moreover, the thermal effects can have significant and deleterious effects on the fibre and its guiding properties that ultimately provide a limit to the reachable output power or lifetime of the fibre laser [25].

Understanding the temperature distribution can therefore be an important aspect of optimising fibre laser designs, especially in the high-power regime. It turns out that this ‘high-power regime’ for mid IR lasers may already be reached with tens of watts, which is significantly lower than hundreds of watts typically observed in near-IR lasers. The two main reasons for this disparity are that the quantum defects are generally much larger in mid-IR lasers, and thermal properties of low-phonon-energy glasses are inferior as compared to fused silica that is almost universally used in the near-IR. In extreme cases such as e.g. in $3\text{ }\mu\text{m}$ lasers, strong water absorption and hygroscopic properties of ZBLAN glass may even lead to runaway thermal runaway effects than limit the lifetime of unprotected fibre tips to only a few hours [26].

Finding the temperature distribution is generally a three dimensional and time-dependent problem, but it can be significantly simplified in most cases of practical importance. Due to the fibre geometry, which is essentially a cylinder where the transverse dimensions are much smaller than the typical length L , the corresponding heat flow in the lateral direction can be neglected in comparison to the transverse direction. Moreover, if we limit our interest to the final temperature during laser operation, then the problem becomes of the steady-state type, even for pulsed operation as long as the repetition rate is much higher than the inverse thermal relaxation time of the fibre, which is of the order of ms to s. Additionally, with the possible exception of fibres with a highly eccentric core, simplification due to radial symmetry can be applied. In Fig. 13.19 a typical fibre cross-section is shown with a core, cladding and coating together with the heat source in the core and the outside boundary condition used in our model formulation.

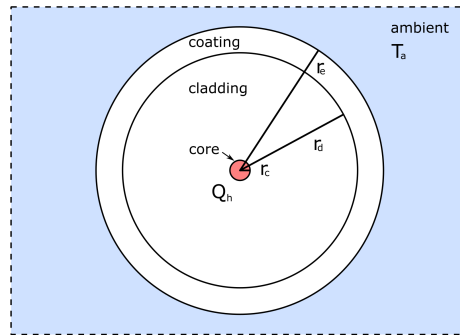


FIGURE 13.19 Geometry in the fibre thermal model with core, cladding and coating domains. The heat source is only in the core (red area) and the ambient defines the boundary condition (blue area).

The fibre temperature can thus be modelled by heat equations expressed in radial coordinates [25], taking the form:

$$\begin{aligned} \frac{k}{r} \frac{\partial}{\partial r} \left(r \frac{\partial T}{\partial r} \right) &= -Q_h, & 0 \leq r \leq r_c, \\ \frac{k}{r} \frac{\partial}{\partial r} \left(r \frac{\partial T}{\partial r} \right) &= 0, & r_c < r \leq r_e, \end{aligned} \quad (13.21)$$

where k is thermal conductivity in the core/cladding ($k_c = k_d \sim 0.7$ W/mK for ZBLAN glass) and coating material ($k_e \sim 0.2$ W/mK for polyacrylate), while Q_h is the heat source density that is confined to the doped core; r_c , r_d and r_e are radii of the core, cladding and coating, respectively.

The boundary conditions in the centre of the fibre ($r = 0$), at the inner interface between the cladding and the coating (at $r = r_d$), and at the fibre coating and ambient interface (at $r = r_e$) can be described as follows:

$$\begin{aligned} \frac{dT}{dr} &= 0, & r &= 0, \\ k_d \frac{dT}{dr} &= k_e \frac{dT}{dr}, & r &= r_d, \\ \frac{dT}{dr} &= \frac{h}{k_e} [T_a - T], & r &= r_e. \end{aligned} \quad (13.22)$$

No heat flow is possible at the very centre due to its symmetry and therefore, the temperature gradient is equal to zero at that point. The heat flow at the fibre external side is determined by the heat transfer coefficient h from the coating to the surrounding medium (e.g. air), assumed at constant ambient temperature T_a . The condition at the inner boundary between the cladding and coating at $r = r_d$ is simply ensuring the required continuity of the heat flow on either side of the interface.

The above equations can be solved analytically, resulting in the the radial distribution for the temperature in the core, the cladding and the coating:

$$\begin{aligned} \Delta T_0 - \frac{Q_h r^2}{4k_c}, & & 0 \leq r \leq r_c, \\ \Delta T(r) = \Delta T_0 - \frac{Q_h r_c^2}{4k_c} \left[1 + 2 \ln \left(\frac{r}{r_c} \right) \right], & & r_c < r \leq r_d, \\ \Delta T_0 - \frac{Q_h r_c^2}{4k_c} \left[1 + 2 \ln \left(\frac{r_d}{r_c} \right) + \frac{2k_d}{k_e} \ln \left(\frac{r}{r_d} \right) \right], & & r_d < r \leq r_e. \end{aligned} \quad (13.23)$$

The maximum temperature increase $\Delta T_0 = \Delta T(r = 0)$ is in the centre of the fibre:

$$\Delta T_0 = \frac{Q_h r_c^2}{4k_c} \left[1 + 2 \ln \left(\frac{r_d}{r_c} \right) + \frac{2k_d}{k_e} \ln \left(\frac{r_e}{r_d} \right) + \frac{2k_e}{hr_e} \right]. \quad (13.24)$$

The heat source power density can be obtained from the absorbed pump power and the fraction of that power that is dissipated as heat. The locally absorbed power can either be obtained from the exponential law using constant absorption coefficient, or from the longitudinal power evolution in the rate equation model. The former is simpler while the latter may be required in the case

of substantial saturation (or bleaching) of the pump absorption when sufficiently high intensities are used. The pump to signal conversion efficiency of the laser can be used as a good practical estimation of the the fractional heat load.

Longitudinal distribution of the temperature difference between the centre of the fibre core and surroundings is plotted in Fig. 13.20 (a), where the exponential form that follows the pump absorption distribution can be recognized. Using the above equations we calculated the radial temperature distribution in the Er:ZBLAN fibre laser setup described in Sec. 13.2.12. The heat source is assumed to be only in the core of the fibre (20 μm diameter), while the 350 μm cladding and 430 μm polymer coating act as passive heat resistance and the surrounding air is the heat drain defined as a boundary condition. The temperature difference between the fibre and its surrounding air is plotted in Fig. 13.20 (b).

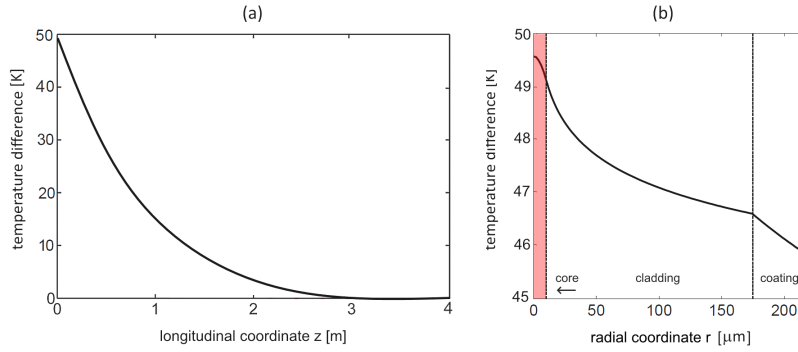


FIGURE 13.20 (a) Longitudinal temperature distribution in the centre of the core ($r = 0 \mu\text{m}$ in Er:ZBLAN fibre laser from Sec. 13.2.12 with 10 W input pump power. (b) Radial temperature distribution at the pump end ($z = 0 \text{ m}$) of the same fibre laser. The core is the heat source (red area) and a free-air boundary condition (blue line) is used, while temperature difference between the surrounding air temperature is shown.

We note that the temperature drop from the core to the outer side of the fibre coating is only about 4 K, but its gradient $\Delta T/\Delta r$ is greater than the longitudinal gradient $\Delta T/\Delta z$ by about three orders of magnitude. The approximation to neglect the lateral heat flow in Eqn. 13.21 is thus well justified. The majority of contribution to the temperature increase, however, appears at the fibre-air boundary, with $h = 80 \text{ W}/(\text{m}^2\text{K})$ as was used in this case.

Knowing the heat transfer coefficient parameter h is therefore of critical importance to obtaining accurate temperatures in the fibre. In air-cooled fibres (or fibre tips suspended in air) the heat flows from the fibre into the surrounding air via natural convection and with thermal radiation. Natural convection is a linear function of temperature difference, and it depends on the air humidity as well as the geometry, size and orientation of the body. The optical fibre

in our case is a horizontally placed cylinder with a diameter in the range of a few hundred μm , and in this range the heat transfer coefficient depends strongly on the diameter [27]. The radiative power of a grey body is described by the Stefan-Boltzmann law and depends on the fourth power of the temperature. It can be linearised in a narrow temperature range of interest above the absolute zero temperature, to form a combined heat transfer coefficient of the form:

$$h = h_0 \left(\frac{r_0}{r_e} \right)^{2/3} + 4e\sigma T_a^3, \quad (13.25)$$

where $h_0 = 50 \text{ W}/(\text{m}^2\text{K})$ and $r_0 = 250 \mu\text{m}$ are constants that were obtained with computational fluid dynamics calculations [28]; e is fibre surface emissivity (~ 0.9 typical for glasses and polymers), σ is the Stefan-Boltzmann constant and T_a ambient air temperature.

The dependence of the combined heat transfer coefficient on the fibre size is plotted in Fig. 13.21(a), where the significant role of the fibre outer (coating) diameter can be observed. It is worthwhile to note that the benefits to cooling in the fibre geometry are thus two folds, firstly by spreading the heat generated in laser operation along the long length of the fibre, and secondly by enabling effective heat removal from the surface due to their small diameters (as compared to e.g. larger and shorter bulk crystals having typical dimension in the mm range and $h \sim 10 \text{ W}/(\text{m}^2\text{K})$).

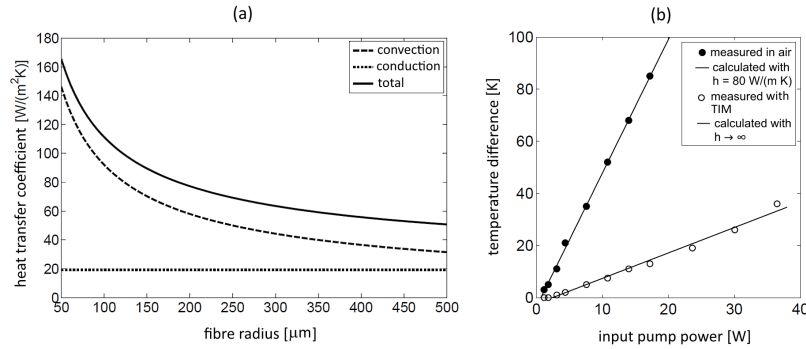


FIGURE 13.21 (a) Calculated heat transfer coefficient due to convection and radiation, depending on the diameter of the fibre outermost layer and temperature, respectively. (b) Measured (dots) and calculated temperatures (lines) at the pumped end of the Er:ZBLAN fibre laser from Sec. 13.2.12 in two cooling conditions, suspended in air and contacted with a thermal interface material (TIM).

Nonetheless, convective cooling still represents the main limit in removing the heat and thus decreasing the temperature of the fibre core. This limit can be greatly alleviated, however, by contacting the fibre surface with materials that have much higher heat conductivity than air, e.g. by immersion in water

or using special thermal interface materials (TIM). In that case the heat transfer coefficient can become large enough to effectively render the last term in Eq. negligible in comparison to the radial heat flow inside the fibre. This condition is achievable in practice even though e.g. water (or many TIMs) have thermal conductivity comparable to that of the ZBLAN ($k \sim 0.7$ W/mK), which is due to cylindrical geometry.

In Fig. 13.21(b) measured and calculated temperatures of the fibre tip are shown at the pump end for the two cooling arrangements, namely with the fibre tip suspended in free air, and also with the same fibre tip contacted with thermal interface material and clamped in a water cooled metal block. The comparison clearly shows that an effective cooling scheme can decrease the core temperature by almost an order of magnitude. We note that similarly effective liquid cooling has been used experimentally to achieve a previous record 24 W output power in a Er:ZBLAN fibre laser [29].

13.4 ULTRAFast MODE-LOCKED LASER MODELLING

The rate equation approach introduced earlier in this chapter is a valuable tool for modelling CW, Q-switched and gain-switched laser emission, where only the intensity of the laser field (i.e. photon flux) is considered. This method, however, is not appropriate for simulating mode-locked lasers, which produce picosecond and femtosecond pulses and are an important class of laser system in their own right.

For these ultrashort pulse durations, other physical phenomena (e.g. dispersion) become important, requiring phase information in addition to intensity information, to accurately describe pulse evolution. The light field can therefore be modelled as an array of complex numbers, representing the time-dependent field amplitude, $A(t)$ on some appropriately chosen numerical grid. Fortunately, due to the timescales of such ultrashort pulses, it is often reasonable to neglect the complex gain dynamics in mode-locked lasers in favour of a simple generic gain model (i.e. not requiring detailed spectroscopic information), and to primarily focus on the dispersive and nonlinear effects that have a more significant role on pulse shaping.

The problem of computing the output from a mode-locked laser thus reduces to the simulation of pulse propagation along fibre, in addition to defining simplified models to describe the action of other cavity components. One could formulate a model that combines the action of all these components lumped into a single equation to describe the whole cavity (e.g. the Haus Master Equation / Ginzburg-Landau Equation [30]), with averaged cavity properties specified as normalised input parameters. However, a more accurate, and conceptually simpler, *piecewise* approach is to consider the effect of each component in turn. The complete simulation procedure is then: begin by generating a initial noise field (e.g. shot noise); propagate this field through the numerical model for each cavity component in turn; after one round-trip, extract some light as the output (i.e.

at an output coupler) and re-inject the remaining light into the first component; repeat this process until the simulated output converges to a steady-state (often, requiring thousands of round trips).

We note that this modelling approach has already been widely studied for near-IR fibre systems (e.g. Refs. [31, 32, 33, 34, 35] and references therein). Practically, the most demanding aspect is solving the nonlinear pulses propagation equation, often in the form of a generalised nonlinear Schrödinger Equation (GNLSE). Practical modelling techniques to solve the GNLSE have also been widely discussed (e.g. using split-step or interaction picture methods; see Ref. [36] for a comprehensive treatment). Therefore, for brevity, we focus here on summarising the nuances of adapting such models for mid-IR fibre lasers, which requires developing models for the relevant properties of mid-IR glasses and components, in addition to consideration of mid-IR specific problems such as atmospheric absorption.

13.4.1 Numerical Models for Mid-IR Components

13.4.1.1 Fibre

For realistic ultrashort pulse simulations, it is essential to provide accurate dispersive and nonlinear properties of the fibre. Short pulses intrinsically possess broad bandwidths, thus it can be important to know these properties at not only a single wavelength, but across the whole region of interest, spanning 10's–100's nm. The fibre's optical properties also depend on which optical mode is excited, although we typically consider only the fundamental LP_{01} mode (i.e. assuming single-mode fibre). Of course, for optimal accuracy the fibre could be directly measured, although it is often preferable to numerically estimate these properties, saving time and enabling new fibre designs to be evaluated.

In this case, for symmetrical step-index fibre geometries, the mode's properties can be described by a characteristic eigenvalue equation, following the seminal work of Snyder and Love [37]. The equation takes as inputs: the core diameter, and refractive index of the core (n_{co}) and cladding (n_{cl}) at a given wavelength λ . The eigenvalue solution is the propagation constant $\beta(\lambda)$, which can be computed across a range of wavelengths to describe the wavelength-dependent phase delay. These β values can be directly included in a frequency-domain GNLSE to account for all dispersive effects, or alternatively, particular dispersion orders (e.g. β_2 is group velocity dispersion, β_3 is third order dispersion etc.) can be found by differentiation: $\beta_n = \frac{d^n \beta}{d\omega^n}$.

This widely used technique is simple to adapt for mid-IR fibres by entering appropriate refractive index values for the fibre's soft glass material. While it should be noted that ZBLAN is a multi-component glass where the exact composition (and thus properties) may vary between manufacturers, reasonable accuracy is obtained using Sellmeier equation coefficients in literature from early

bulk glass measurements. The refractive index is thus given by:

$$n^2(\lambda) = 1 + \sum_j \frac{A_j \lambda^2}{\lambda^2 - B_j^2} \quad (13.26)$$

where for ZBLAN, $A_1 = 1.22514$, $A_2 = 1.52898$ and $B_1 = 0.08969 \mu\text{m}$, $B_2 = 21.3825 \mu\text{m}$ [38]. The difference between core and cladding index is specified by the fibre manufacturer, often in terms of numerical aperture, $\text{NA} = \sqrt{n_{\text{co}}^2 - n_{\text{cl}}^2}$. Therefore, by inputting only the core diameter and NA of any mid-IR step-index fibre, alongside appropriate Sellmeier coefficients, it is possible to compute the full dispersion profile.

This technique also enables determination of the fibre's nonlinear parameter, γ , which is defined as:

$$\gamma(\lambda) = \frac{2\pi}{\lambda} \frac{n_2}{A_{\text{eff}}(\lambda)} \quad (13.27)$$

where n_2 is the (approximately wavelength independent) material's nonlinear index and A_{eff} is the effective mode area. $A_{\text{eff}}(\lambda)$ can be found by integrating over the field amplitude originating from the eigenmode analysis, e.g. defined in Ref. [37], or more simply, by applying the approximate Marcuse equation [39]. For the inherent material nonlinearity, n_2 values reported for ZBLAN in the literature show a degree of variation, from 2.1×10^{-20} to $5.4 \times 10^{-20} \text{ m}^2/\text{W}$, although we note that $n_2 = 2.1 \times 10^{-20}$ is widely used, following a recent study comparing ZBLAN experiments and simulations [40].

Pulse shaping in mode-locked lasers is dominated by interplay between γ and β , thus the above fibre model is often sufficient for simulating ultrashort pulse generation. Under certain circumstances (e.g. long fibre lengths / very high peak powers), however, additional nonlinear effects such as stimulated Raman scattering can become important. Studies of near-IR femtosecond lasers have shown that while such phenomena can typically be neglected, when cavities are designed for maximum peak power, Raman-driven destabilisation can occur [41], requiring the inclusion of the fibre's Raman gain profile for accurate simulations. Therefore, mid-IR mode-locked laser simulations could be further augmented by including numerical models for Raman gain in ZBLAN fibres, e.g. as discussed in Refs. [40, 42]. Finally, while we have focussed on ZBLAN fibre, one could model fibre of any material using the same approach, simply by providing the associated Sellmeier coefficients and nonlinearity values.

13.4.1.2 Gain Medium

Amplification in rare-earth-doped ultrafast fibre lasers can be simulated by including gain $g(\lambda)$ in the GNLSE. While one could compute gain values and the exact position-dependent gain shape (based on the population inversion) from detailed rate equations each round-trip (as presented in the first part of this chapter), the computational cost would be high. Additionally, in many mode-locked

lasers, cavity phenomena such as fibre dispersion or other added components place more restrictive limits on pulse narrowing (i.e. preventing spectral broadening) than gain filtering anyway. Despite the fact that mid-IR transitions are typically complex (i.e. requiring ESA or ETU), Ref. [43] showed (for an 2.8 μm Er:ZBLAN laser) that a simple saturable gain model (as widely used for near-IR mode-locked laser modelling) is a good estimation. In this case, the gain is defined as:

$$g(\lambda) = \frac{g_0}{1 + E_p/E_{\text{sat}}} \times S(\lambda) \quad (13.28)$$

where E_{sat} is the saturation energy (which is varied to simulate changing the amplifier pump power), $E_p = \int |A(t)|^2 dt$ is the simulated pulse energy, g_0 is the small-signal gain and $S(\lambda)$ is the spectral profile of the gain. g_0 can be estimated beforehand from a CW rate equation analysis (since in both CW and mode-locking operating states, once a steady-state is reached, the gain does not change with time) or alternatively can be adjusted empirically to calibrate the model against existing experimental datasets. $S(\lambda)$ can be defined by a Lorentzian line shape, centred at the known emission wavelength of the ion and with full width at half maximum (FWHM) set equal to the width of the ASE spectrum that is measured from the fibre of interest when pumped, thus simulating the finite gain bandwidth [43].

13.4.1.3 Saturable Absorber

A saturable absorber, which is commonly used to passively modulate cavity light to generate ultrashort pulses, can be described by an intensity $I(t) = |A(t)|^2$ dependent transfer function (i.e. acting instantaneously on the pulse) with transmission (so $A_{\text{out}} = \sqrt{T}A_{\text{in}}$):

$$T(I) = 1 - \frac{\alpha_0}{1 + I/I_{\text{sat}}} - \alpha_{\text{ns}} \quad (13.29)$$

where α_0 is the modulation depth, I_{sat} is the saturation intensity and α_{ns} is the non-saturable loss (which can be directly measured or obtained from the saturable absorber manufacturer).

Thus far we have considered a scalar optical field $A(t)$, which assumes a fixed linear polarisation (i.e. using all-polarisation-maintaining (PM) fibre). This approach has been widely shown to yield good experimental agreement, even with lasers constructed from non-PM components. For the case of non-PM lasers, this can be explained since an adjustable polarisation controller is often included in experiments to compensate for uncontrolled cavity birefringence. However, for added accuracy and to simulate polarization-based mode-locking phenomena (e.g. nonlinear polarisation evolution, NPE), a vector-based GNLSE can be employed which propagates two fields along the fibre, $A_x(t)$ and $A_y(t)$ accounting for the two polarization modes and their interaction [43, 44].

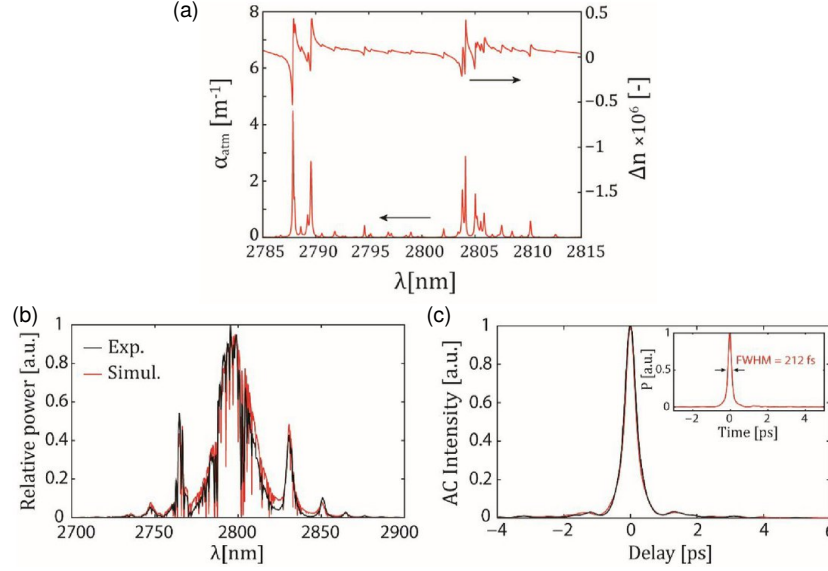


FIGURE 13.22 (a) Atmospheric absorption coefficient and induced modification in refractive index around 2.8 μm . Comparison of experimental and simulated (b) optical spectrum and (c) autocorrelation trace of a mode-locked Er:ZBLAN fibre laser. From Ref. [43], © SPIE.

13.4.2 Impact of Atmospheric Absorption

The presence of numerous atmospheric molecular absorption lines in the mid-IR region results in an additional pulse shaping effect in mid-IR mode-locked cavities that include free-space sections. In this case, numerical modelling is useful tool to understand the impact of such features [43, 45].

First, absorption data can be obtained from the comprehensive HITRAN molecular spectroscopic database [46]. This absorption leads to both a wavelength-dependent reduction in light intensity and a phase delay, where the phase delay can be computed based on the change in air's refractive index according to the Kramers-Kronig relations [Fig. 13.22(a)]. Free-space sections can then be described with complex transmission matrix T :

$$T = \exp \left(-L_{\text{atm}} \left(\frac{i\omega}{c} n(\omega) + \frac{1}{2} \alpha_{\text{atm}}(\omega) \right) \right) \quad (13.30)$$

where L_{atm} is the free-space section length, $n(\omega) = 1 + \Delta n(\omega)$ is the modified atmospheric index due to absorption and α_{atm} is the atmospheric absorption coefficient [43].

13.4.3 Mode-Locked Laser Modelling Applications

The techniques outlined in this section have been practically applied to numerous mid-IR lasers, with agreement between simulations and experiments validating the methods. For example, Ref. [43] studied one of the first femtosecond mode-locked $2.8\text{ }\mu\text{m}$ Er:ZBLAN fibre lasers, which generated 270 fs pulses with 23 kW peak power. Using simulations based on a GNLSE with a simplified gain model, and also including atmospheric absorption, optical spectra and autocorrelation traces were numerically computed that captured detailed features of the experiment [Fig. 13.22(b)–(c)]. Notably, this included sharp spectral dips corresponding to absorption lines. The simulated output showed 22.8 kW peak power and 212 fs pulse duration, in reasonable agreement with experimental values.

A major benefit of simulations is the ability to selectively disable certain physical phenomena in the model, thus isolating the impact of each effect. Interestingly, by contrasting simulations performed with/without atmospheric absorption, Ref. [43] showed that these absorption features increased the number of round-trips required after turn-on before the laser converged to stable operation, particularly for short fibre lengths. Such observations are critical to guiding future laser designs and we note that Ref. [44] has also recently considered the optimisation of Er:ZBLAN mode-locked lasers through detailed modelling.

An additional successful application of numerical simulations was the proposal/demonstration of *frequency shifted feedback* mode-locking in a Dy:ZBLAN fibre laser, tunable from 2.97 to $3.3\text{ }\mu\text{m}$ [47]. Here, the inclusion of an intracavity AOTF led to a frequency shift each round trip, enabling pulse generation without the need for a saturable absorber. By including a numerical frequency shift and bandpass filtering effect in the laser cavity model, simulations were able to accurately predict the laser output, in addition to revealing new details about the pulse formation process.

13.5 CONCLUSIONS AND OUTLOOK

Computational models are an invaluable tool in mid-IR fibre laser research and development. At the most basic level, the rate equation approach provides a description of the ionic population dynamics under the influence of optical excitation and subsequent emission. Rate equation modelling has therefore been shown to be ideal for estimating important laser performance metrics, subject to spectroscopic data inputs and cavity design parameters. With these tools, researchers have been able to optimize laser designs using numerical optimization routines, with significantly lower cost and shorter timescales than equivalent laboratory-based experimentation alone.

The utility of rate equation modelling extends beyond laser design using known rare-earth transitions, however. By comparing experimental and numerical observations, researchers have been able to use their models to estimate

unknown spectroscopic quantities, such as ETU coefficients and ESA cross sections, which can be otherwise challenging to measure directly. With sustained research efforts to push fibre lasers to even longer wavelengths, rate equation models are therefore critical to the discovery and understanding of new laser transitions. For example, a room-temperature 4 μm fibre laser has recently been demonstrated using Ho:ZBLAN [48], following numerical investigations that elucidated ESA and ETU as pathways to overcome the self-terminating nature of the transition [49]. Much further work still remains to understand how to optimize these new 4 μm lasers. There is also intense research activity in the development of doped chalcogenide fibres for even longer wavelength emission, supported by many positive numerical modelling studies [50].

One of the main challenges in mid-IR rate equation modelling is that, apart from the simple case of the in-band-pumped Dy, mid-IR lasers typically rely on spectroscopically complex transitions between high-lying levels in an ion's energy level structure. As a result, numerous levels and many excitation/relaxation pathways must be considered, leading to complicated systems of equations. While one can always consider high-performance computing (HPC) facilities for such problems, for widespread practical exploitation of laser modelling tools, it is preferable for simulations to be completed on non-specialist hardware and within reasonable time frames.

As with all simulations, a trade-off exists between model accuracy and the computational cost of finding solutions. Therefore, various approaches have been discussed in this chapter to simplify the problem while retaining the core physics. An additional aspect is the importance of structuring the problem in a format which is amenable to solution by high-performance algorithms. The matrix formulation of rate equations is one such example as it enables efficient linear algebra techniques to be employed. It is foreseeable that future theoretical advantages could offer additional simplifications to the mathematical formalism, in addition to new algorithms for finding solutions.

Advances in the field of computer science and technology could also impact on laser modelling more generally. Beyond the obvious benefit of continual increases in processing power and more widespread access to cloud / HPC computing, advances in machine intelligence are particularly worthy of note. Neural networks and other machine learning approaches are already being widely deployed across many areas of science, leading to the development of systems that learn to solve problems based on large datasets, rather than being explicitly programmed. The application of such approaches to rate equation modelling could potentially lead to automated agents for developing optimized lasers, without even needing to provide the underlying physical atomic description / full spectroscopic data. This is definitely a fruitful area for future work.

While this chapter has primarily focussed on rate equation modelling, we also discussed thermal simulations and mode-locked laser modelling, which are complementary tools that will enable scaling mid-IR fibre lasers to even higher powers and operating in ultrashort pulsed regimes. Future modelling trends and

advances will certainly also apply to these techniques, in addition to many other optical simulation concepts (e.g. modelling individual optical components such as mid-IR FBGs and fibre couplers) which are beyond the scope of this Chapter. Without doubt, optical simulations have played a key role in the significantly enhanced performance that has been reported from mid-IR fibre lasers over the past decade and with improved models, this trend can only continue.

Bibliography

- [1] M. Gorjan, M. Marinček, M. Čopič, Role of interionic processes in the efficiency and operation of erbium-doped fluoride fiber lasers, *IEEE J. Quantum Electron.* 47 (2) (2011) 262–273. doi:10.1109/JQE.2010.2073447.
- [2] J. Li, L. Gomes, S. D. Jackson, Numerical modeling of holmium-doped fluoride fiber lasers, *IEEE J. Quantum Electron.* 48 (5) (2012) 596–607. doi:10.1109/JQE.2012.2188380.
- [3] F. Maes, V. Fortin, M. Bernier, R. Vallee, Quenching of 3.4 μm dual-wavelength pumped erbium doped fiber lasers, *IEEE J. Quantum Electron.* 53 (2) (2017) 1600208. doi:10.1109/JQE.2017.2677383.
- [4] R. I. Woodward, M. R. Majewski, D. D. Hudson, S. D. Jackson, Swept-wavelength mid-infrared fiber laser for real-time ammonia gas sensing, *APL Photonics* 4 (2019) 020801. doi:10.1063/1.5065415.
- [5] A. Malouf, O. Henderson-Sapir, M. Gorjan, D. J. Ottaway, Numerical modeling of 3.5 μm dual-wavelength pumped erbium-doped mid-infrared fiber lasers, *IEEE J. Quantum Electron.* 52 (11) (2016) 1600412.
- [6] R. I. Woodward, M. R. Majewski, N. Macadam, G. Hu, T. Albrow-Owen, T. Hasan, S. D. Jackson, Q-switched Dy:ZBLAN fiber lasers beyond 3 μm : comparison of pulse generation using acousto-optic modulation and inkjet-printed black phosphorus, *Opt. Express* 27 (10) (2019) 15032–15045. doi:10.1364/OE.27.015032.
- [7] A. E. Siegman, *Lasers*, University Science Books, 1986.
- [8] C. Giles, E. Desurvire, Modeling erbium-doped fiber amplifiers, *J. Light. Technol.* 9 (2) (1991) 271–283. doi:10.1109/50.65886.
- [9] G. C. Valley, Modeling Cladding-Pumped Er / Yb Fiber Amplifiers, *Opt. Fiber Technol.* (2001) 21–44.
- [10] R. Paschotta, *RP Photonics: Fiber Amplifiers Tutorial* (2019). URL https://www.rp-photonics.com/tutorial_fiber_amplifiers.html
- [11] M. J. F. Digonnet, M. K. Davis, R. H. Pantell, Rate equations for clusters in rare earth-doped fibers, *Opt. Fiber Technol.* 1 (1994) 48.
- [12] W. T. Carnall, H. M. H. Crosswhite, H. M. H. Crosswhite, Energy level structure and transition probabilities in the spectra of the trivalent lanthanides in LaF_3 , 1978. doi:10.2172/6417825.

- [13] M. P. Hehlen, M. G. Brik, K. W. Krämer, 50th anniversary of the Judd-Ofelt theory: An experimentalist's view of the formalism and its application, *J. Lumin.* 136 (2013) 221–239. doi:10.1016/j.jlumin.2012.10.035.
- [14] R. Reisfeld, Radiative and non-radiative transitions of rare-earth ions in glasses, Vol. 22, 1975. doi:10.1007/BFb0116557.
- [15] C. Barnard, P. Myslinski, J. Chrostowski, M. Kavehrad, Analytical model for rare-earth-doped fiber amplifiers and lasers, *IEEE J. Quantum Electron.* 30 (8) (1994) 1817–1830. doi:10.1109/3.301646.
- [16] W. H. Press, S. A. Teukolsky, W. T. Vetterling, B. P. Flannery, *Numerical Recipes: The Art of Scientific Computing*, 2007.
- [17] J. Kierzenka, L. F. Shampine, A BVP solver based on residual control and the Matlab PSE, *ACM Trans. Math. Softw.* 27 (3) (2001) 299–316. doi:10.1145/502800.502801.
- [18] R. I. Woodward, M. R. Majewski, G. Bharathan, D. D. Hudson, A. Fuerbach, S. D. Jackson, Watt-level dysprosium fiber laser at 3.15 μm with 73% slope efficiency, *Opt. Lett.* 43 (7) (2018) 1471–1474. doi:10.1364/OL.43.001471.
- [19] P. Golding, S. Jackson, T. King, M. Pollnau, Energy transfer processes in Er^{3+} -doped and $\text{Er}^{3+}, \text{Pr}^{3+}$ -codoped ZBLAN glasses, *Phys. Rev. B* 62 (2) (2000) 856–864. doi:10.1103/PhysRevB.62.856.
- [20] M. Pollnau, S. D. Jackson, Energy recycling versus lifetime quenching in erbium-doped 3- μm fiber lasers, *IEEE J. Quantum Electron.* 38 (2) (2002) 162–169. doi:10.1109/3.980268.
- [21] O. Henderson-Sapir, J. Munch, D. J. Ottaway, New energy-transfer upconversion process in Er^{3+} :ZBLAN mid-infrared fiber lasers, *Opt. Express* 24 (7) (2016) 6869. doi:10.1364/OE.24.006869.
- [22] O. Henderson-Sapir, J. Munch, D. J. Ottaway, Mid-infrared fiber lasers at and beyond 3.5 μm using dual-wavelength pumping, *Opt. Lett.* 39 (3) (2014) 493–496.
- [23] O. Henderson-Sapir, A. Malouf, N. Bawden, J. Munch, S. D. Jackson, S. Member, D. J. Ottaway, Recent advances in 3.5 μm erbium-doped mid-infrared fiber lasers, *IEEE J. Sel. Top. Quantum Electron.* 23 (3) (2017) 0900509.
- [24] J. Li, S. D. Jackson, Numerical Modeling and Optimization of Diode Pumped Heavily-Erbium-Doped Fluoride Fiber Lasers, *IEEE J. Quantum Electron.* 48 (4) (2012) 454–464. doi:10.1109/JQE.2012.2183856.

54 BIBLIOGRAPHY

- [25] D. C. Brown, H. J. Hoffman, Thermal, stress, and thermo-optic effects in high average power double-clad silica fiber lasers, *IEEE J. Quantum Electron.* 37 (2) (2001) 207–217.
- [26] N. Caron, M. Bernier, D. Faucher, R. Vallée, Understanding the fiber tip thermal runaway present in 3 μm fluoride glass fiber lasers., *Opt. Express* 20 (20) (2012) 22188. doi:10.1364/OE.20.022188.
- [27] F. P. Incropera, D. P. DeWitt, T. L. Bergman, A. S. Lavine, *Fundamentals of Heat and Mass Transfer*, Wiley, 2011.
- [28] M. Gorjan, M. Marinček, M. Čopič, Pump absorption and temperature distribution in erbium-doped double-clad fluoride-glass fibers, *Opt. Express* 17 (22) (2009) 19814. doi:10.1364/oe.17.019814.
- [29] S. Tokita, M. Murakami, S. Shimizu, M. Hashida, S. Sakabe, Liquid-cooled 24 W mid-infrared Er:ZBLAN fiber laser, *Opt. Lett.* 34 (20) (2009) 3062–3064. doi:10.1364/OL.34.003062.
- [30] H. A. Haus, Mode-locking of lasers, *IEEE J. Sel. Top. Quantum Electron.* 6 (6) (2000) 1173–1185. doi:10.1109/2944.902165.
- [31] R. Paschotta, Noise of mode-locked lasers (Part I): numerical model, *Appl. Phys. B* 79 (2) (2004) 153–162. doi:10.1007/s00340-004-1547-x.
- [32] E. Ding, W. H. Renninger, F. W. Wise, P. Grelu, E. Shlizerman, J. N. Kutz, High-energy passive mode-locking of fiber lasers, *Int. J. Opt.* 2012 (2012) 354156. doi:10.1155/2012/354156.
- [33] I. A. Yarutkina, O. V. Shtyrina, M. P. Fedoruk, S. K. Turitsyn, Numerical modeling of fiber lasers with long and ultra-long ring cavity, *Opt. Express* 21 (10) (2013) 12942. doi:10.1364/OE.21.012942.
- [34] A. F. J. Runge, C. Agüergaray, R. Provo, M. Erkintalo, N. G. R. Broderick, All-normal dispersion fiber lasers mode-locked with a nonlinear amplifying loop mirror, *Opt. Fiber Technol.* 20 (6) (2014) 657–665. doi:10.1016/j.yofte.2014.07.010.
- [35] R. I. Woodward, Dispersion engineering of mode-locked fibre lasers [Invited], *J. Opt.* 20 (2018) 033002. doi:10.1088/2040-8986/aaa9f5.
- [36] J. C. Travers, M. H. Frosz, J. M. Dudley, Nonlinear fibre optics overview, in: J. M. Dudley, J. R. Taylor (Eds.), *Supercontinuum Generation in Optical Fibers*, Cambridge, 2010.
- [37] A. W. Snyder, J. Love, *Optical Waveguide Theory*, Chapman and Hall Ltd, 1983.

- [38] F. Gan, Optical properties of fluoride glasses: a review, *J. Non. Cryst. Solids* 184 (1995) 9–20. doi:10.1016/0022-3093(94)00592-3.
- [39] D. Marcuse, Loss analysis of single-mode fiber splices, *Bell Syst. Tech. J* 56 (5).
- [40] C. Agger, C. Petersen, S. Dupont, H. Steffensen, J. K. Lyngsø, Carsten L. Thomsen, J. Thøgersen, S. Rud Keiding, O. Bang, Supercontinuum generation in ZBLAN fibers - detailed comparison between measurement and simulation, *J. Opt. Soc. Am. B* 29 (4) (2012) 635–645.
- [41] C. Aguerarary, A. Runge, M. Erkintalo, N. G. R. Broderick, Raman-driven destabilization of mode-locked long cavity fiber lasers: fundamental limitations to energy scalability, *Opt. Lett.* 38 (15) (2013) 2644. doi:10.1364/OL.38.002644.
- [42] S. Duval, M. Olivier, L.-R. Robichaud, V. Fortin, M. Bernier, M. Piché, R. Vallée, Numerical modeling of mid-infrared ultrashort pulse propagation in Er³⁺:fluoride fiber amplifiers, *J. Opt. Soc. Am. B* 35 (6) (2018) 1450. doi:10.1364/josab.35.001450.
- [43] S. Duval, M. Olivier, V. Fortin, M. Bernier, M. Piché, R. Vallée, 23-kW peak power femtosecond pulses from a mode-locked fiber ring laser at 2.8 μm , *Fiber Lasers XIII Technol. Syst. Appl.* 9728 (2016) 972802. doi:10.1117/12.2204746.
- [44] F. Zhang, W. Yan, S. Liang, C. Tan, P. Tang, Numerical study on the soliton mode-locking of the Er³⁺-doped fluoride fiber laser at $\sim 3 \mu\text{m}$ with nonlinear polarization rotation, *Photonics* 6 (1) (2019) 25. doi:10.3390/photonics6010025.
- [45] M. Gebhardt, C. Gaida, F. Stutzki, S. Hädrich, C. Jauregui, J. Limpert, A. Tünnermann, Impact of atmospheric molecular absorption on the temporal and spatial evolution of ultra-short optical pulses, *Opt. Express* 23 (11) (2015) 13776. doi:10.1364/OE.23.013776.
- [46] I. E. Gordon, E. al, The HITRAN2016 molecular spectroscopic database, *J. Quant. Spectrosc. Radiat. Transf.* 203 (2017) 3–69. doi:10.1016/j.jqsrt.2017.06.038.
- [47] R. I. Woodward, M. R. Majewski, S. D. Jackson, Mode-locked dysprosium fiber laser: picosecond pulse generation from 2.97 to 3.30 μm , *APL Photonics* 3 (11) (2018) 116106. doi:10.1063/1.5045799.
- [48] F. Maes, V. Fortin, S. Poulain, M. Poulain, J.-Y. Carree, M. Bernier, R. Vallée, Room-temperature fiber laser at 3.92 μm , *Optica* 5 (7) (2018) 761–764.

56 BIBLIOGRAPHY

- [49] L. Gomes, V. Fortin, M. Bernier, F. Maes, R. Vallée, S. Poulain, M. Poulain, S. D. Jackson, Excited state absorption and energy transfer in Ho ³⁺ -doped indium fluoride glass, *Opt. Mater.* 66 (2017) 519–526. doi:10.1016/j.optmat.2017.02.048.
- [50] Ł. Sójka, Z. Tang, H. Zhu, E. Bereś-Pawlik, D. Furniss, A. B. Seddon, T. M. Benson, S. Sujecki, Study of mid-infrared laser action in chalcogenide rare earth doped glass with Dy³⁺, Pr³⁺ and Tb³⁺, *Opt. Mater. Express* 2 (11) (2012) 1632. doi:10.1364/OME.2.001632.